# Visualization and characterization of liquid water saturation in polymer electrolyte membrane gas diffusion layers via *operando tomography*

By

Leya Kober

A thesis submitted in conformity with the requirements for
the degree of Master of Applied Science

Department of Mechanical and Industrial Engineering
University of Toronto

# Visualization and characterization of liquid water saturation in polymer electrolyte membrane gas diffusion layers via *operando tomography*

Leya Kober

Master of Applied Science

Department of Mechanical and Industrial Engineering

University of Toronto

2025

## Abstract

Polymer electrolyte membrane (PEM) fuel cells offer a promising pathway toward reducing reliance on carbon-emitting energy technologies. However, their widespread implementation is hindered by high costs, primarily attributed to mass transport losses during high current density operation caused by inefficiencies in liquid water management. This thesis comprises two studies that characterize liquid water saturations at the pore scale of the gas diffusion layer (GDL) and their impact on performance. First, pore-scale saturation is defined for the first time through visualization techniques, revealing that pores are partially saturated rather than fully saturated, and local saturation in the bulk GDL influences pore saturation. Next, the impact of reactant gas relative humidity (RH) on liquid water saturation and PEM fuel cell performance is determined. Local saturation was observed to increase with RH, leading to a corresponding rise in pore saturation. This thesis provides insight into the design of new, more efficient materials for improved PEM fuel cell performance.

## Acknowledgements

To Professor Aimy Bazylak, thank you for your mentorship, encouragement, and unfaltering support. Your kindness, patience, and dedication to my success mean the world to me. You inspire me every day.

To Tina, Vasant, Lijun, Tess, Raymond, Harsharaj, Aida, Spencer, Dhruvi, Jason, Josh, Alexandre, Salvatore, Beste, and Ashley, thank you for making the lab a warm, welcoming environment. I will always remember the fun that we had over the last few years, and I wish you all the greatest success.

To Pranay and Eric, thank you for being incredible mentors throughout this degree. Your wisdom and guidance have been invaluable, inspiring me to dedicate myself to lifelong learning every day.

To Abby, Lexi, Hallie, Maybi, Natalie, and Gabriel, thank you for your unwavering love and support. Even on my darkest days, you always managed to put a smile on my face and remind me that I am worthy of the enduring camaraderie that each of you gives.

To Basit, thank you for the endless laughs and devoted companionship during the long, sleepless nights spent writing this thesis. You turned some of the toughest moments into treasured memories.

To Grandma, thank you for your words of encouragement and for always believing in me.

To Dad, thank you for your encouragement and support. You inspired me to pursue engineering; I would not be where I am without you. I strive to embody the strength and intelligence that define you.

To Mom, thank you for being my lifeline. Without your friendship, your sacrifices, and your unwavering commitment to my healing, I could not be the person that I am today.

# Table of Contents

# List of Tables

# List of Figures

# Abbreviations and Nomenclature

## Technical Abbreviations

| | |
|---|---|
| CCM | Catalyst coated membrane |
| CL | Catalyst layer |
| CT | Computed tomography |
| FF | Flow field |
| FIB-SEM | Focused ion beam-scanning electron microscopic |
| GDL | Gas diffusion layer |
| GHG | Greenhouse gas |
| MEA | Membrane electrode assembly |
| MPL | Microporous layer |
| OCV | Open-circuit voltage |
| PEM | Polymer electrolyte membrane |
| PEN | Polyethylene naphthalate |
| PN | Pore network |
| PNM | Pore network modelling |
| PTFE | Polytetrafluoroethylene |
| RH | Relative humidity |
| ROI | Region of interest |
| XTM | X-ray tomographic microscopy |

## Nomenclature

| | |
|---|---|
| $\gamma$ | Surface tension |
| $D$ | Diffusivity in gas |
| $D_{eff}$ | Effective bulk-gas diffusivity |
| $\theta$ | Contact angle |
| $P_c$ | Capillary pressure [Pa] |
| $r$ | Pore radius |
| $S_L$ | Local saturation |
| $S_P$ | Pore saturation |
| $S_{P,avg}$ | Average pore saturation |
| $\tau$ | Tortuosity |
| $V_{P,E}$ | Volume of empty pore |
| $V_{P,F}$ | Volume of empty space in pore after water invasion |
| $V_{P,W}$ | Volume of "wet" pores |
| $V_V$ | Volume of void space |
| $V_W$ | Volume of water |
| $\varphi$ | Porosity |

# Chapter 1 – Introduction

## 1.1 Preamble

While energy demands are continually increasing worldwide, there is also a competing, pressing need to shift away from carbon-emitting energy sources due to anthropogenic climate change. Alternative energy technologies are critically needed to meet our energy demands without contributing further to carbon emissions [1]. While solar and wind power have been widely implemented to address these challenges, they are intermittent sources that fluctuate with local environmental conditions [2]. Polymer electrolyte membrane (PEM) fuel cells are promising for providing green, on-demand electricity due to their ability to provide on-demand, zero-emission, and continuous electric power when supplied with hydrogen fuel and oxygen from air, producing only water and heat as by-products [3]. The transportation sector is an ideal target for PEM fuel cell applications as it was the second largest source of greenhouse gas emissions (GHGs) in 2022 [4]. PEM fuel cells are an appealing alternative to conventional internal combustion engine vehicles not only for the elimination of harmful GHGs but for their high efficiency, high power output, and scalability [5]. However, the implementation of PEM fuel cells is not without its own challenges; high costs related to materials and performance efficiency at high current density operation are an obstacle to their widespread adoption [6].

The gas diffusion layer (GDL), a thin, porous carbon fibre material, is an integral part of the fuel cell as it facilitates the diffusion of reactants to reaction sites at the catalyst layer (CL) as well as the transport of product liquid water out of the fuel cell. At high current densities, fuel cell performance is primarily limited by mass transport losses, where inadequate reactant delivery hinders the continuation of electrochemical reactions due to excess liquid water in the pores of the

GDL. While efforts need to be made to reduce liquid water saturation in the GDL to mitigate mass transport losses, a water balance must be maintained in the cell to obtain sufficient hydration of the PEM in order to preserve ionic conductivity for efficient reactions. Thus, effective water management strategies are imperative to improving PEM fuel cell performance.

## 1.2 Objectives

The objective of this thesis is to identify the mechanisms governing water transport at the pore scale within the cathode GDL of a PEM fuel cell to help inform the design of new materials for more efficient water management with the goal of reducing mass transport losses. By reducing mass transport losses, PEM fuel cells can operate more efficiently and at higher current densities for a wider range of applications. This objective will be achieved through the following sub-objectives:

1. To visualize liquid water distributions at the pore scale to better understand water transport mechanisms in the GDL. By improving the understanding of liquid water movement in the GDL, we can inform the design of new materials for more effective water management in the fuel cell.
2. To determine the impact of inlet gas relative humidity (RH) on liquid water distributions in the GDL at the pore scale and on PEM fuel cell performance. By deducing the role of RH in water transport mechanisms, we can provide insight into more efficient operating conditions for improved PEM fuel cell performance.

## 1.3 Contributions

### 1.3.1 First-authored journal manuscripts

This thesis comprises two studies, currently being prepared as first-authored manuscripts, detailed as follows:

- **L. Kober**, P. Shrestha, E. Chadwick, C. T. Ham, S. Gasilov, A. Webb, A. Bazylak, "*Distinction and* relationship between local and pore-scale saturation in fuel cell gas diffusion layers clarified via *high-speed operando tomography*," (*in preparation for journal submission*, Chapter 4)
- **L. Kober**, P. Shrestha, E. Chadwick, S. Gasilov, A. Webb, A. Bazylak, "Identifying relationships between inlet gas relative humidity and liquid water saturation in polymer electrolyte membrane gas diffusion layers via *operando tomography*," (*in preparation for journal submission*, Chapter 5)

These studies were completed with the support of research members from the Thermofluids for Energy and Advanced Materials (TEAM) lab at the University of Toronto. Pranay Shrestha assisted with the design of the experimental hardware and experiments. Eric Chadwick assisted with experiments and provided feedback on data analysis. Additionally, Dr. Adam Webb, Dr. Ning Zhu and Dr. Sergey Gasilov from the Canadian Light Source provided administrative and operational support for the X-ray computed tomography experiments.

### 1.3.2 Co-authored manuscripts

- C. T. Ham, P. Shrestha, **L. Kober**, S. Gasilov, A. Webb, A. Bazylak, "Identifying Temperature-dependent Pore-scale Gas Transport in PEM Electrolyzers using Operando X-ray Computed Tomography," (*in preparation for journal submission*)

### 1.3.3 Conference presentations and abstracts

- **L. R. Kober**, P. Shrestha, C. T. Ham, and A. Bazylak, "Investigating the Capability of High-speed Operando Sychrotron X-ray Computed Tomography to Image Porous Materials in Fuel Cells: An Optimized Fuel Cell Design", *17th International Symposium on Polymer Electrolytes*, Oct. 2-7, 2022.
- **L. Kober**, P. Shrestha, C. Ham, and A. Bazylak, "Investigating the Influence of Humidity on Liquid Water Transport Mechanisms in Fuel Cell Gas Diffusion Layers Using Operando X-Ray Computed Tomography," ECS Meeting Abstracts, vol. MA2022-02, p. 1411, Oct. 2022, doi: 10.1149/MA2022-02391411mtgabs.
- **L. Kober**, P. Shrestha, S. Lytle, and A. Bazylak, "Investigating the Influence of Inlet Relative Humidity on Polymer Electrolyte Membrane Fuel Cell Performance by Visualizing 4-D Water Distributions in Gas Diffusion Layers," ECS Meeting Abstracts, vol. MA2023-02, p. 1785, Dec. 2023, doi: 10.1149/MA2023-02371785mtgabs.

## 1.4 Thesis Organization

This thesis is organized into six chapters. In Chapter 1, a high-level background into PEM fuel cells is provided. Additionally, this chapter describes the motivation for visualizing liquid water distributions at the pore scale in cathode GDLs. Chapter 2 provides a thorough literature review on PEM fuel cells including the chemistry, components, water transport mechanisms, and mass transport losses within them. Chapter 3 details the methodology used to carry out experiments as well as the methods used for image processing and data analysis for Chapters 4 and 5. In Chapter 4, the impact of local saturation on pore-scale saturation is investigated by applying the methodology in Chapter 3 to visualize pore-scale water in the GDL. In Chapter 5, the impact of RH on pore-scale water distributions and PEM fuel cell performance is determined by applying the methodology presented in Chapter 3 to visualize liquid water distributions at the pore scale and connect them to performance. Finally, Chapter 6 provides a summary of the contributions of the studies presented in Chapters 4 and 5 and presents recommendations for future work.

# Chapter 2 – Background

This chapter provides a detailed background on polymer electrolyte membrane (PEM) fuel cells to establish context for the research contributions presented in this thesis. An overview of PEM fuel cell operation is presented first, followed by a description of its components and their influence on performance. Finally, a review of imaging and modelling techniques used in the elucidation of water transport mechanisms in PEM fuel cell gas diffusion layers is provided.

## 2.1 An overview of the PEM fuel cell

The PEM fuel cell is an electrochemical energy conversion device that converts chemical energy into useful electricity through the reactions of hydrogen and oxygen at the catalyst layer (CL) (commonly platinum) of an ionically conductive catalyst-coated membrane (CCM). The internal components of the PEM fuel cell make up the membrane electrode assembly (MEA) which consists of a CCM placed between two porous electrodes, the anode and the cathode, which are then encased by bipolar plates (Figure 2-1).

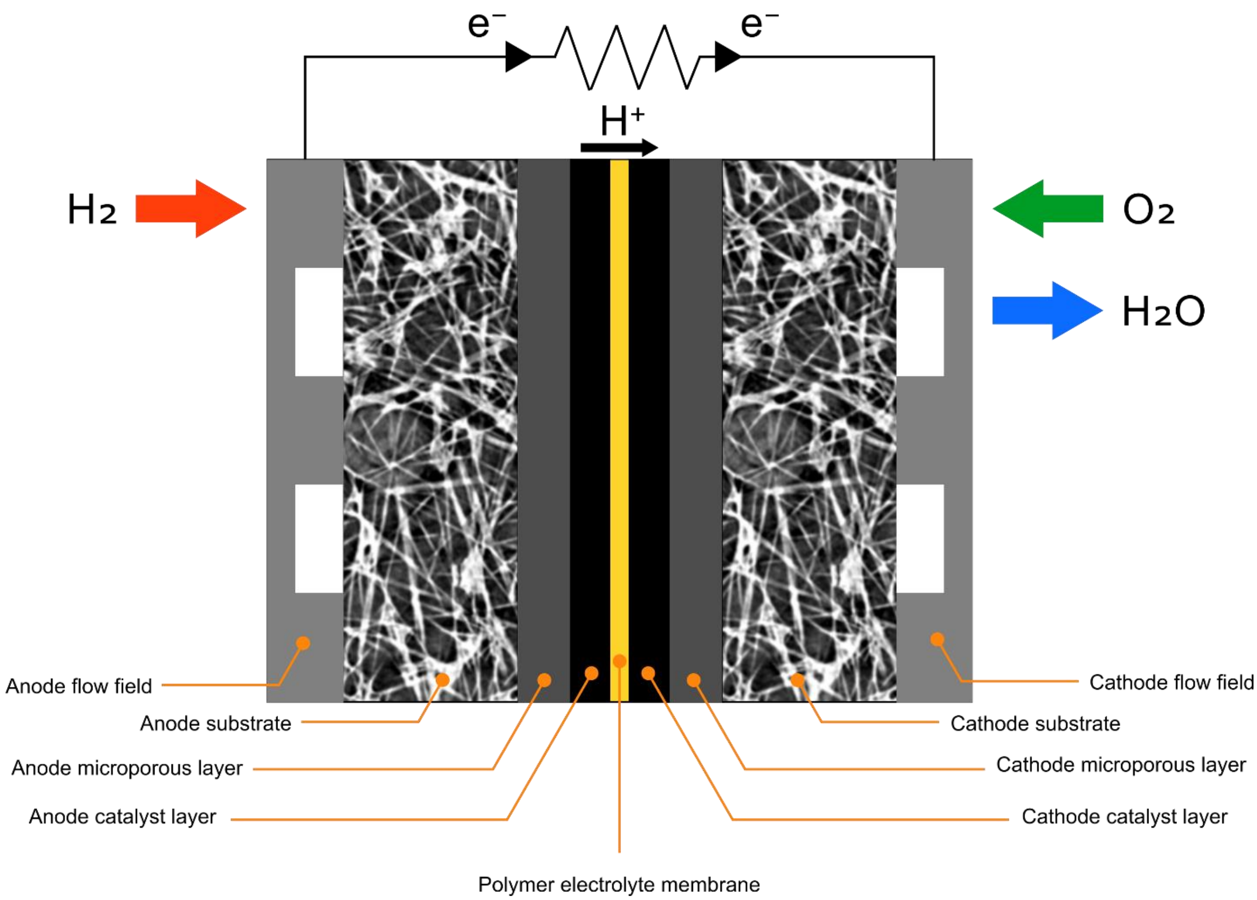


**Figure 2-1**: Schematic showing cross-section of a PEM fuel cell.

The anode and cathode facilitate the half-cell reactions that make up the complete reaction within the cell, where gaseous hydrogen and oxygen combine to produce water. At the anode, the half-cell reaction is referred to as the oxidation reaction, where hydrogen is oxidized at the CL to produce 2 protons ($H^+$) and 2 electrons ($e^-$):

$$H_2 \rightarrow 2H^+ + 2e^- \tag{2.1}$$

The protons are conducted through the PEM while the electrons travel to an external circuit to power a device. At the cathode, the half-cell reaction is referred to as the reduction reaction, where oxygen is oxidized by combining with the conducted hydrogen protons and the electrons from the external circuit to produce water and heat:

$$\frac{1}{2}O_2 + 2H^+ + 2e^- \rightarrow H_2O \tag{2.2}$$

Combined, these half-cell reactions form the following complete reaction that occurs within the cell:

$$H_2 + \frac{1}{2}O_2 \rightarrow H_2O \tag{2.3}$$

## 2.2 Components of the PEM fuel cell

In this section, the components that make up a typical PEM fuel cell will be discussed in detail to help provide context for their role in the operation of the cell.

### 2.2.1 Catalyst-coated membrane

The CCM is a tri-layer structure at the centre of the PEM fuel cell that consists of a PEM coated with a catalyst layer that is bound together by an ionomer. While it facilitates the reactions in the cell, it also acts as a barrier between the anode and the cathode.

#### 2.2.1.1 Polymer electrolyte membrane

The PEM is a thin, solid, and selectively permeable material which selectively conducts protons ($H^+$) from the anode to the cathode in the hydrogen oxidation reaction while providing electrical insulation between the electrodes. It maintains gas separation between the cathode and anode to prevent fuel crossover which can lead to cell inefficiencies and safety issues [7]. It also provides mechanical support to prevent deformation under compressive stress in the cell with varying operating conditions, including changes in temperature and humidity [8]. The most commonly used PEM is Nafion, which is a sulfonated tetrafluorethylene-based fluoropolymer with two main components, (1) hydrophobic backbone made of polytetrafluoroethylene (PTFE) that provides chemical resistance, mechanical strength, and hydrophobicity, and (2) hydrophilic side chains that contain sulfonic acid groups that ionize in the presence of water, forming mobile protons and facilitating proton conduction [9]. The advantages of using Nafion include high proton conductivity under well-hydrated conditions, excellent chemical and mechanical stability, and well-established manufacturing process and widespread availability. Sufficient hydration of the PEM is key to maintaining high proton conductivity, so water management in PEM fuel cells is of the utmost importance.

#### 2.2.1.2 Catalyst layer

The CL is typically a layer of nanometer-sized particles of platinum dispersed on a carbon support. Supported platinum catalyst particles are bound together by a proton-conducting ionomer, which facilitates the oxidation of hydrogen molecules on the anode side of the PEM fuel cell and the reduction of oxygen on the cathode side of the cell [10]. The proton-conductive ionomer binder allows protons to travel through the catalyst layer to the PEM, which then transports them to the cathode reaction sites.

### 2.2.2 Gas diffusion layer

The gas diffusion layer (GDL), a porous, often heterogeneously structured material, is instrumental in the operation of a PEM fuel cell as it facilitates the diffusion of reactant gases to the CL and the transport of liquid water away from the CL. It is commonly composed of an electronically conductive carbon-based substrate and in some cases, is coated with a microporous layer (MPL) made up of carbon black mixed with a hydrophobic binder (e.g., PTFE) [11]. It is critical for GDLs to be made of electronically conductive material in order to provide a conductive pathway for electrons between the CL and the bipolar plates. It also provides mechanical support for the thin CL and PEM, preventing deformation under compressive loads in the cell. While the presence of water is necessary in maintaining proton conductivity of the PEM, excess water in the GDL can lead to flooding and performance loss in the PEM fuel cell due to the blockage of oxygen to reaction sites [12]. Thus, the substrate material is typically coated with a hydrophobic binder, such as PTFE, to assist with effective water management and prevent flooding [13]. Understanding liquid water transport in the GDL is paramount in order to optimize the GDL structure and design more efficient fuel cells; therefore, it is often an area of interest in fuel cell research.

### 2.2.3 Bipolar plates

Also known as flow fields, these electrically conductive structural supports are situated on the side of the GDL opposite to the catalyst layer and are used to deliver reactants and expel product water from the fuel cell. The bipolar plates are manufactured with void spaces known as channels which provide pathways for species to move relatively unimpeded in and out of the fuel cell. The solid material surrounding the channels are known as the lands, which are in direct contact with the GDL substrate so that electrons produced at the CL can be transported to an external circuit. During fuel cell operation, product water has been known to accumulate mostly under the land regions rather than under the channels, due to their manufacture from hydrophilic materials and smaller pore sizes induced by compression [14], [15].

## 2.3 Water transport mechanisms in the GDL

In this section, we discuss the physics that governs vapour and liquid phase water transport in the GDL. Water transport in the GDL involves complex interactions between liquid and vapour phases. These processes are driven by capillary forces, phase change dynamics, diffusion, and pressure gradients. Liquid water is generated at the cathode as a byproduct of the oxygen reduction reaction, while water vapour is present in the cell at the CL/GDL interface due to the evaporation of liquid water as a result of exothermic reactions and humidified reactant gases supplied to the cell.

### 2.3.1 Liquid water phase water transport in the GDL

Capillary transport is widely considered the dominant mechanism for liquid water transport in the GDL [16]. Capillary pressure ($P_c$) drives liquid water through the pores and is inversely proportional to pore radius ($r$):

$$P_c = -\frac{2\gamma \cos\theta}{r} \tag{2.4}$$

where $\gamma$ is the surface tension of water and $\theta$ is the contact angle of water to the surface, which determines hydrophobicity. To facilitate water transport and alleviate potential flooding, the GDL is generally coated with a hydrophobic treatment, such as PTFE, which alters the surface energy of the porous structure, affecting the capillary pressure [17]. In work by Nam et al. and Pasaogullari et al., the transport of liquid water from the membrane to the GDL is presented as an "upside-down tree" capillary network, where a high number of small capillary networks evenly dispersed across the membrane converge into larger capillaries and eventually results in one large capillary reaching breakthrough at the GDL/flow field interface [18], [19]. However, Litster et al. discovered that liquid water transport is instead dominated by capillary fingering and channeling and features numerous "dead-ends", where water transport in capillaries recedes when an adjacent breakthrough channel is formed [16]. Bazylak et al. identified that liquid water follows preferential pathways as a result of localized hydrophilic pathways in the bulk hydrophobic GDL that are induced by compressive damage at the GDL surface due compressive stresses on the GDL [20]. At the pore scale, liquid water preferentially occupies larger and more hydrophilic pores [21], [22].

### 2.3.2 Vapour-phase water transport in the GDL

The dominant mechanism for gas-phase transport in the GDL is diffusion, where vapour molecules diffuse to different parts of the GDL as a result of concentration gradients [23]. These concentration gradients are induced in the GDL because of the thermal gradient from the CL to the flow fields [23], [24] due to the heat generated at the CL interface during the exothermic electrochemical reactions and condensation at the flow fields.

For gas-phase flow in porous media, such as the GDL, the properties of the porous media, such as porosity and tortuosity, affect the rate of diffusion through the media which is often inhibited. Porosity is a measurement of the void space in a material and is defined as the ratio between the volume of the void space to the total volume of the material [25]. Tortuosity is a measure of convolution in path length in porous media compared to the linear path length across the media in the direction of transport. The more tortuous the path, the longer the path length and the greater the reduction in effective diffusivity [26].

The effective diffusivity for gas-phase flow in porous media can be represented as

$$D_{eff} = D\frac{\varphi}{\tau} \tag{2.5}$$

where $D_{eff}$ is the effective bulk-gas diffusivity, $D$ is the diffusivity in gas, $\varphi$ is the porosity, and $\tau$ is the tortuosity.

The addition of an MPL to the GDL has been shown to enhance vapour transport by decreasing thermal conductivity and increasing temperatures at the CL [27], [28]. However, the addition of an MPL leads to an unavoidable increase in diffusion path length, increasing tortuosity and decreasing effective diffusion across the cathode [29].

## 2.4 Mass transport losses

Mass transport losses in the PEM fuel cell occur when reactant gas flow to the CL is impeded, typically by the liquid water produced at the CL in the cathode from the oxygen reduction reaction. Mass transport losses are intensified with increasing current density because higher reaction rates, needed for greater electrical output, lead to increased liquid water production. In order to reduce mass transport losses, effective water management strategies must be employed to ensure effective reactant delivery to the CL. One method for managing water in the GDL is the addition of an MPL, which is a layer with sub-micron sized pores placed on the CL/GDL interface side of the cell. The addition of an MPL to GDL substrate has shown to make significant improvements in the management of liquid water in the GDL, where liquid water removal is enhanced and liquid saturation in the catalyst layer is reduced, allowing the cell to operate at higher current densities [30]. Understanding liquid water transport mechanisms is key for developing more efficient water management strategies and can assist in the development of new materials for reduced mass transport losses.

## 2.5 Visualization techniques for fuel cell materials

A popular method used to understand water transport mechanisms in the GDL is visualization through imaging techniques. X-ray radiography is one technique that can provide useful information about water accumulation in the GDL. In x-ray radiography, a 2-dimensional (2-D) image of the internal structure of the GDL is produced which captures the layers and structures in a single plane, compressing three-dimensional information into a flat image with high temporal resolution for high-speed measurements. Previous studies have used X-ray radiography to contribute valuable information on liquid water evolution and accumulation within the cathode GDL [31-34]. Hinebaugh et al. used synchrotron x-ray radiography to study the time evolution of liquid water in an operating PEM fuel cell; they observed that liquid water first appeared at the cathode catalyst layer and then travelled laterally (in-plane direction) across the land and channel regions, and that liquid water accumulated in possible areas of delamination of the GDL from the CL [35]. Antonacci et al. used a combination of electrochemical impedance spectroscopy (EIS) and synchrotron X-ray radiography to observe changes in GDL water content over time with increasing current density and found that water content increased with current density until a threshold where increases in current density did not impact local liquid water content in the GDL [36]. While X-ray radiography has proven to provide important insight into the behaviour of water in the GDL, the loss of depth information limits our knowledge in the third dimension and prevents us from observing separate water clusters and water within individual pores.

X-ray computed tomography (CT) is a non-destructive imaging technique that generates a 3-dimensional (3-D) image of a sample and has been employed in numerous PEM fuel cell studies for its ability to provide detailed information about the complete internal structure of the GDL and water at the pore scale [37-41]. X-ray CT has been used to image cells *operando* to analyze dynamic processes of fluids in GDLs. Eller et al. used X-ray tomographic microscopy (XTM), a type of X-ray CT that specializes in high spatial resolution, on an *operando* cell to observe liquid water at technically relevant conditions and analyzed the distribution of water cluster size and connectivity [42]. They identified four different types of water clusters in the GDL substrate based on connectivity and found that water clusters under the channels drain directly into the channels and do not grow above a certain volume of water, while under the lands water clusters of much higher volume accumulate. Dörenkamp et al. also used XTM to study the transient development and interaction of multiple percolating water clusters in a GDL as well as droplet formation in the channels. They found that there are transient instabilities in developed percolating water networks, and the disconnection between a droplet and its feeding cluster can lead to the sudden removal of large volumes of water into the channels, which can open up intermediate pathways for improved reactant transport [43].

## 2.6 Pore network modelling for water transport

Pore network modelling (PNM) is a popular technique used for modelling pore-scale water transport within the GDL. In these models, porous media is represented by a network of pores interconnected via cylindrical throats where the geometric characteristics of the media are maintained, such as pore diameter, throat diameter, and pore volume [44]. In PEM fuel cell research, pore networks are often developed from X-ray CT images of GDLs to accurately represent the geometry and use the results of experimental studies to validate the model. PNM is desirable for modelling pore-scale dynamics due to its relative accuracy that is comparable to other techniques while it demands a lower computational cost [45], [46]. Shahraeeni et al. developed a PNM based on patterns of liquid water flow inside the GDL in previous studies [47], [48]. They measured flow rates numerically to estimate water saturation in both untreated and PTFE treated GDLs, and found that in thin GDLs, the addition of a hydrophobic agent improves fuel cell performance by reducing GDL saturation, however in thick GDLs, the effect of hydrophobic treatment is insignificant [49]. Aghighi et al. applied a PNM to the cathode GDL to investigate mechanisms leading to liquid water formation in the cell and were able to predict the phase change of water under varying operating conditions. Their work shows that spatial temperature and vapour gradients lead to the condensation of water in colder zones of the cathode, especially under the lands. PNMs have also been employed to investigate the effects of the presence of an MPL on liquid water transport [50]. Nakajima et al. constructed a PNM with the aid of focused ion beam-scanning electron microscopic (FIB-SEM) observation of the 3-D structure of an MPL through pore size distribution. They simulated air and liquid water permeabilities as well as oxygen diffusivities in the MPL intruded with water [51]. From these studies, the insight gained from PNM in the prediction of multiphase water flow coupled with its low computational cost shows its value in the investigation of water transport in the GDL.

## 2.7 Chapter Summary

In this chapter, a comprehensive background on PEM fuel cells, including electrochemistry, important components, and water transport mechanisms, was discussed. Mass transport losses were introduced, along with their impact on PEM fuel cell performance, highlighting the importance of studies in water transport mechanisms in the GDL. Next, techniques for visualizing liquid water in PEM fuel cells were introduced, where methods such as X-ray CT are discussed as valuable methods for characterizing pore-scale transport of liquid water. Finally, PNM approaches for modelling multi-phase flow in the GDL were discussed with key examples of its capabilities.

In this thesis, X-ray CT was used simultaneously with electrochemical testing of an *operando* fuel cell to visualize pore-scale water distributions in the cathode GDL and characterize their impact on performance; the methodology used to achieve this is presented in Chapter 3. In Chapter 4, we focus on a phenomenon known as partial pore filling, where pores in the GDL substrate exhibit saturations less than 1, which is often not accounted for in modelling. We explore the link between local saturation conditions in the bulk GDL and partial pore filling and the potential impacts that this has on our understanding of pore-scale liquid water distributions. In Chapter 5, we evaluate the effects of inlet gas relative humidity on partial pore filling regimes and investigate the formation of new water transport pathways. The work in this thesis provides a better understanding of water transport mechanisms at the pore scale in the GDL, which can help inform the development of new GDL materials for enhanced liquid water management.

# Chapter 3 – Methodology

## 3.1 Introduction

This chapter describes the methodology used to isolate 3-dimensional (3-D) water distributions generated in the GDL substrate of the *operando* polymer electrolyte membrane (PEM) fuel cell used in the experiments conducted in Chapters 4 and 5. In this chapter, we first describe the details of the imaging setup and settings used to capture X-ray computed tomography (CT) images of the PEM fuel cell active area. We then provide the details of the PEM fuel cell including the hardware and materials used across experiments. Finally, we discuss the image acquisition process and the details of the image processing techniques used to extract pore-scale data from our X-ray CT images for analysis, including image reconstruction, subtraction, and segmentation. The methodology for determining local and pore saturation in the GDL substrate with the use of a pore network is detailed in both Chapters 4 and 5 for the corresponding experiments.

## 3.2 X-ray CT imaging settings

X-ray computed tomography imaging was conducted at the 05B1-1 bending magnet beamline in the Biomedical Imaging and Therapy (BMIT) facility at the Canadian Light Source (CLS) in Saskatoon, Canada [52]. The PEM fuel cell (Figure 3-1a) was mounted on a flat stage and oriented in the in-plane direction of the X-ray beam (membrane electrode assembly (MEA) parallel to filtered white beam, energy level 33 keV). Low energy photons were removed from the beam by employing a 0.8 mm-thick aluminum filter. After passing through the cell, a LuAG scintillator (50 μm thickness) (WE Micro, Opt. Peter) transformed the transmitted X-ray irradiance into visible light which was then captured by a scientific complementary metal-oxide-semiconductor (sCMOS) camera (Marana, Andor). For steady state investigation of liquid water distributions, the camera captured 2000 2-dimensional (2-D) tomographic projections of the MEA over 180 ° of rotation at an exposure time of 20 ms, resulting in a total scan time of 40 s per CT image. The images captured a field of view (FOV) of 650 x 2048 px (1.59 x 5.0 mm) at a pixel size of 2.44 µm. Before conducting experiments, flat field images of the beam were taken with the sample absent to correct for bright spots in the beam in image reconstruction. Dark frames were also collected with the beam off to correct for camera noise in reconstruction.

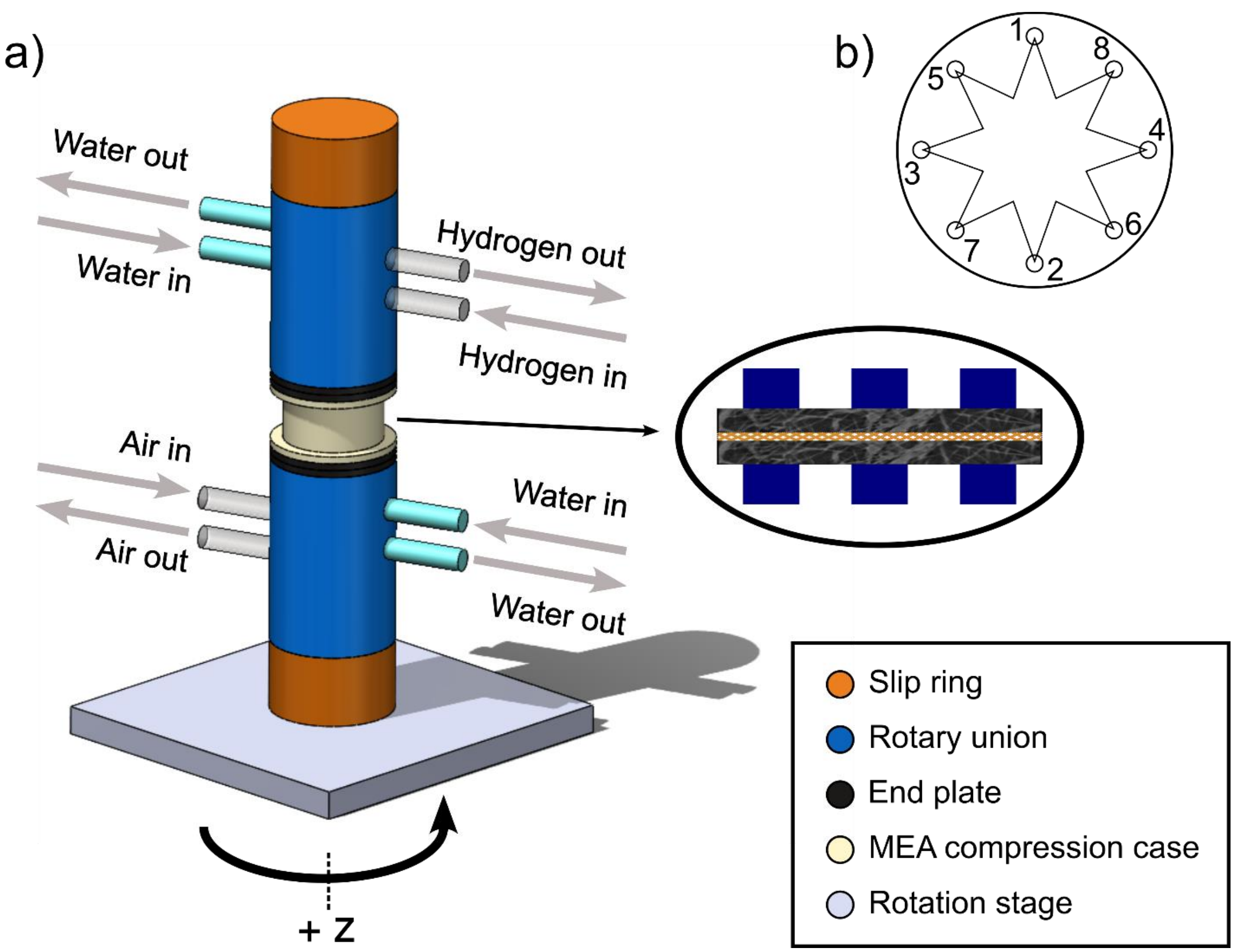


**Figure 3-1**: (a) A schematic of the novel fuel cell with custom-made rotary unions and slip rings for seamless rotation during computed tomography. The tubing / electrical connections to and from

the rotatory unions / slip rings remain stationary during rotation of the central imaging cell, allowing for continuous rotation of the cell. The +*z* axis is the axis of rotation for the cell. (b) The star pattern used to secure the compression case to the end plate, where screws are secured in the order starting with 1 and ending in 8.

## 3.3 Cell design and materials

To acquire a three-dimensional (3D) image of the materials and the processes which occur within a fuel cell, a custom fuel cell (Figure 3-1) was designed and assembled specifically for the purposes of X-ray CT. The current cell design features a small active area to facilitate high-resolution pore-scale imaging (micron-scale resolution) with complete capture of the active area within the field of view of the camera. Specifically, the active area was 3.0 mm x 2.4 mm (0.072cm$^2$) to fit within the field of view of 650 x 2048 pixels at the desired pixel resolution of 2.44 µm.

The fuel cell (Figure 3-1a) features graphite flow fields, copper current collectors, and machined Aluminum 6061 end plates and end plate adapters. End plate adapters were introduced in the design to facilitate the connection of the other cell components to the rotary unions on each end of the cell. The rotary unions are directly connected to the electrical slip rings, with the other end of the cathode slip ring attached to the aluminum mounting plate which rotates. Corrosion and scratch resistance were two parameters heavily considered in this design, as carbon corrosion can lead to reduced cell electrochemical performance and durability [53], [54]. To combat this issue, the current collectors were electroplated with hard gold (16 microinch gold over 55 microinch nickel) to provide corrosion resistance while maintaining electrical conductivity, and the aluminum end plates and adapters were hard anodized for corrosion and scratch resistance.

A noteworthy aspect of the new cell design is the inclusion of heated water lines for highly precise cell temperature control. Water channels are embedded in the end plate adapters where water is circulated through the cell using a circulating heated water bath (Fisherbrand Isotemp 4100). The cell temperature is accurately measured through a T-type thermocouple (Omega Engineering, Inc.) located just underneath the active area in the cathode bipolar plates.

### 3.3.1 Rotary unions and slip rings for continuous cell rotation

To prevent flooding in the cathode gas diffusion layer (GDL), water management techniques can be optimized through informed material design [55], [56]. This information can be achieved by enhancing the understanding of liquid water transport mechanisms in the GDL, which in turn can be accomplished by observing the transient behaviour of water. To reveal transient transport mechanisms, high temporal resolution in imaging is necessary. Continuous rotation enables fast acquisition of consecutive scans without the need to stop cell rotation, providing high temporal resolution across multiple scans.

In previous iterations of our CT cell [57], continuous rotation was difficult to achieve due to the wrapping of gas and heating tubes, as well as electrical wires, around the cell structure as the cell rotated on the CT stage. As a result, very few complete consecutive rotations were possible with the cell attached to the stage, limiting the temporal resolution of the collected data. In our new design, rotary unions and slip rings were selected as a solution to the issue of cell rotation. Figure 3-1a shows the strategic placement of a rotary union and slip ring on each side of the cell, each containing one inner piece that rotates along a rotational axis (shown as the +*z* axis in Figure 3-1a) and an outer piece that remains stationary. This is implemented in the current CT cell design by connecting the gas and water lines to the stationary portion of the rotary union and the electrical connections to the stationary electrical wiring of the slip ring. The portion of the cell between the rotary unions, which encompasses the region of interest, rotates along the axis of rotation of the CT stage along with the internal components of the rotary unions and slip rings. The stationary parts of the cell are fixed to the stationary part of the stage via rigid steel posts. As the innermost part of the cell rotates with the stage, fluid lines and wiring remain stationary and do not invade the field of view.

### 3.3.2 Sealing case for uniform compression

A critical aspect of the small-scale fuel cell design is the compression and sealing of the gas diffusion layer. The current cell design features a rounded, hollow case which encompasses the active area and is bolted to the end plates via a symmetrical flange on both sides (shown in yellow in Figure 3-1a). The bolts are equally spaced around the outer circular portion of the case, which, when tightened carefully and gradually following a star pattern (Figure 3-1b), apply a uniform and sufficient amount of compression to the membrane electrode assembly (MEA) within the active area. Uniform and sufficient compression is vital to the proper performance of a fuel cell as it limits the potentially drastic mass transport losses that incur due to fuel crossover and reduces contact resistance as well as uneven gas distribution [58-60]. In addition to the structural design, polyetheretherketone (PEEK) was selected for the compression case because it did not deform under the torque induced by the cell rotation and was transparent to the white beam, providing beam access to the active area materials.

To determine the quality of GDL compression, an in-plane cross-sectional view of the MEA structure in the assembled fuel cell was analyzed (Figure 3-2). Through this view, ideal compression is identified by the absence of gaps between the GDL, catalyst coated membrane (CCM), and flow field channels, and over-compression is indicated by a significant deformation of the CCM as well as the GDL being forced into the channels. Figure 3-2 demonstrates an example of relatively even, ample compression.

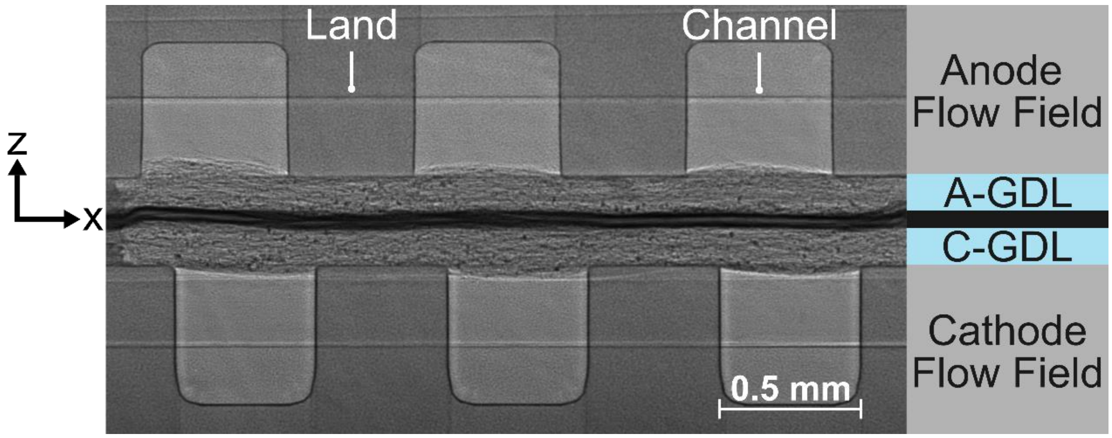


**Figure 3-2**: 2D radiograph showing a vertical cross-sectional view of the compressed membrane electrode assembly between the flow field channels for a fuel cell build with Toray 060 10% wt. GDL.

### 3.3.3 Cell materials

Between the current collectors, graphite flow fields with 3 parallel channels (0.5 mm wide, 0.5 mm deep) separated by lands (0.5 mm wide) were employed. A 5-layer MEA was fitted between the flow fields and consisted of a Nafion™ NR211 catalyst coated membrane (CCM) with a loading of 0.3 mg Pt·cm$^{-2}$ on both the anode and cathode sides of the cell (Ion Power, USA). The gas diffusion layer (GDL) selected for both the cathode and anode was 10% Wet Proofed Toray 060 Carbon Paper (2.4 x 3.0 mm, 190 µm thickness) (Fuel Cell Store, USA) and was sealed on the outer edges by 150 µm-thick polyethylene naphthalate (PEN) gasket sheets for ~20% compression of the GDL.

## 3.4 Image reconstruction

To find the centre of rotation and reconstruct the collected 2-D tomographic projections into 3-dimentional (3-D) image stacks, the UFO-tofu software kit (EZ-UFO), an in-house graphical user interface by the CLS, was utilized [61]. Prior to reconstruction, dark and flat field corrections were applied by subtracting the averaged dark field image from the image stack and then dividing the intensities in the dark-corrected image by the averaged flat field image. Next, phase retrieval, which computes and applies a Fourier filter to correct phase-shifted data [62], was enabled in EZ-UFO to improve contrast between phases and assist with segmentation. The "finding large spots" filter was applied to remove bright spot artifacts by finding large spots with extreme values in the images. Ring removal, which utilizes a PIV filter that generates ring patterns, was enabled in EZ-UFO to remove ring artifacts. Finally, the filtered back projection algorithm, which first uses a 1D projection filter to enhance high frequencies and dampen low frequencies and then spreads the filtered projection data back into the image, was used to reconstruct the volume [63].

## 3.5 Image pre-processing

After reconstruction, pre-processing was completed using ImageJ (open-source image processing software) [64] to rotate, crop, and adjust the contrast of the image stacks. Each image stack was rotated to the same position to assist with future image registration. The reconstructed images were cropped from 2048 x 2048 x 650 px (5.0 x 5.0 x 1.59 mm) to 1130 x 882 x 53 px (2.76 x 2.15 x 0.13 mm) to obtain a representative sample of the cathode GDL for analysis [65]. The intensity threshold of the images was then adjusted to increase the contrast of the images and improve segmentation. The images were then converted to 8-bit for further processing.

## 3.6 Segmentation of liquid water

To segment water in our reconstructed CT scans, we performed an image subtraction between a saturated image and a dry reference image of the same GDL. However, for subtraction to be an effective process to isolate water distributions in saturated images, the dry reference and saturated image must be perfectly aligned. Across CT scans, sample movement and/or deformation can occur, and images may not be at the same rotation angle. To solve this problem and ensure alignment, we used image registration methods to apply a series of transformations to one image to match the position of the other image, which remained stationary. If sample deformation is not expected, rigid transformations can be applied to an image, such as translation, rotation, or scaling. However, in this case rigid transformations were not sufficient, and a non-rigid technique, called simpleitk demons registration, was implemented through Dragonfly software (Object Research Systems) [66].

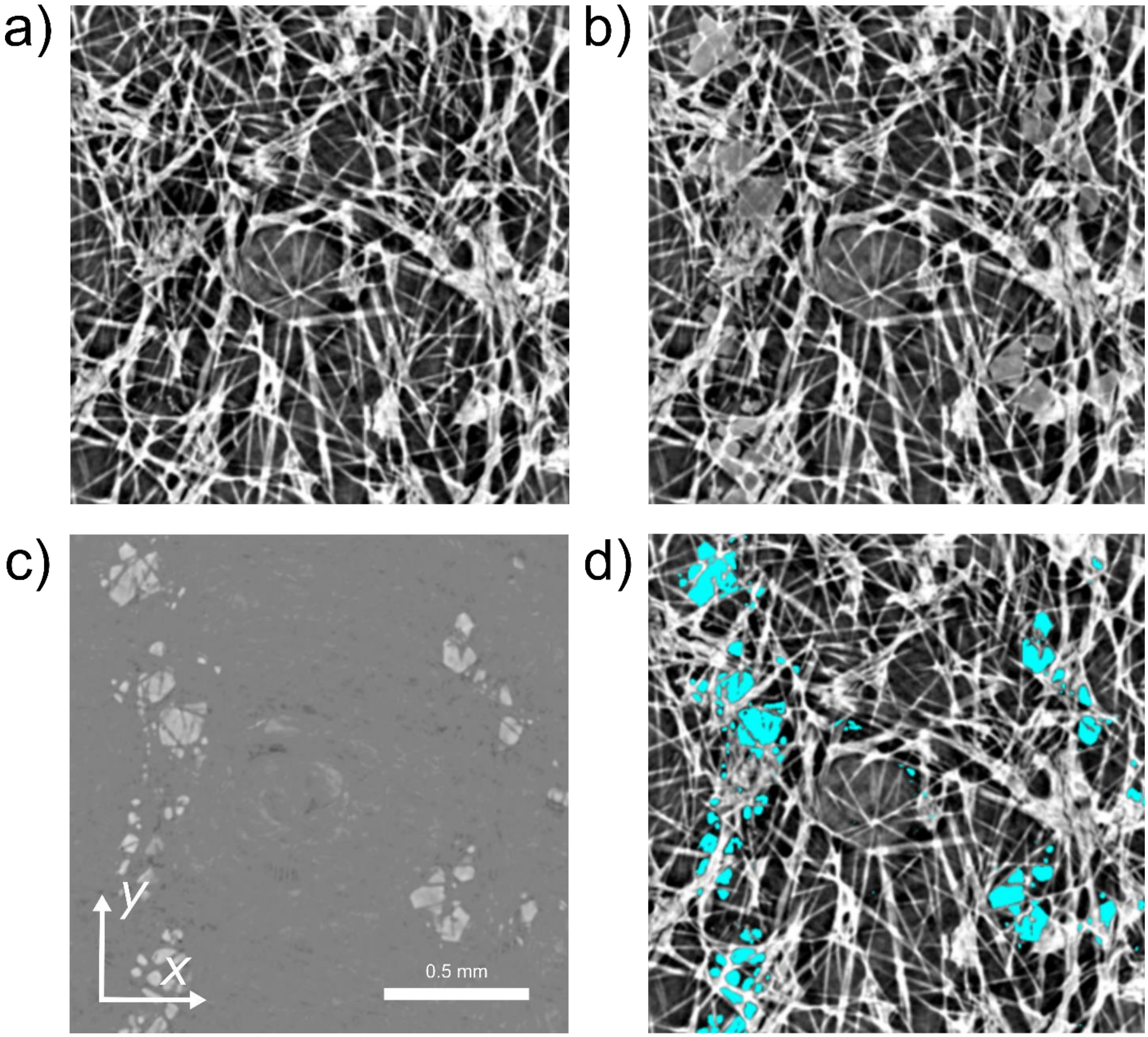


**Figure 3-3**: A 2-D cross-sectional image slice of the cathode GDL at a depth of 65.9 μm from the cathode CL to showcase the image processing procedure used to segment water: (a) OCV reference image, (b) *operando* image of GDL at 2.0 $A{\cdot}cm^{-2}$ current load and 90% RH aligned with (a) using simpleitk demons registration in Dragonfly, (c) isolated liquid water as a result of subtracting (a) from (b), and (d) water (cyan) which has been filtered and segmented from (c) and superimposed on dry OCV image (grayscale) to show water distribution. White scale bar in (a) represents a length of 0.5 mm. Images are taken with a pixel resolution of 2.44 μm.

The simpleitk demons registration method iteratively computes the displacement field which will map a moving image onto a fixed image, where a displacement field is an image whose pixel type is some vector type with a number of elements equal to the dimension of the fixed image [67]. After registration, the fixed, dry reference image (Figure 3-3a) was subtracted from the registered, saturated image (Figure 3-3b) to isolate the water present in the saturated image. The subtraction process involved taking two images as an input and producing a new output image. Each pixel of this new output image was calculated as the difference between corresponding pixel values of the first and second images. The output pixels are given by:

$$Q(i,j) = P_1(i,j) - P_2(i,j) \tag{3.1}$$

where $Q(i,j)$ are the pixels of the output, $P_1(i,j)$ are the pixels of the saturated image and $P_2(i,j)$ are the pixels of the dry reference.

The resulting output image was the isolated water present in the GDL in the saturated state (Figure 3-3c), which could then be easily segmented into void space and water and superimposed onto the segmented dry reference GDL to observe water in the pore space of the GDL (Figure 3-3d).

## 3.7 Segmentation of fibres and void space

To prepare for the generation of a pore network for extracting pore-scale information of the dry and saturated GDL substrate, segmentation of the fibres from the void space was necessary. We began by taking a dry reference image (humidified flow of air and hydrogen at OCV) (Figure 3-4a) of the GDL and applying a 3-D median filter with a 3-pixel radius in ImageJ to smooth the image and reduce the effects of noise for improved segmentation of the fibres from the void space

(Figure 3-4b). The median filter was chosen over a mean filter, as it often preserves details and edges in the image more effectively. The median filter achieved this by looking at the nearby neighbours of each pixel and deciding whether each pixel is representative of its surroundings. It then replaced the pixel value with the median of the surrounding values, which was done in a 3x3 square in all three directions (X, Y, Z) for the case of the 3-D median filter in Fiji.

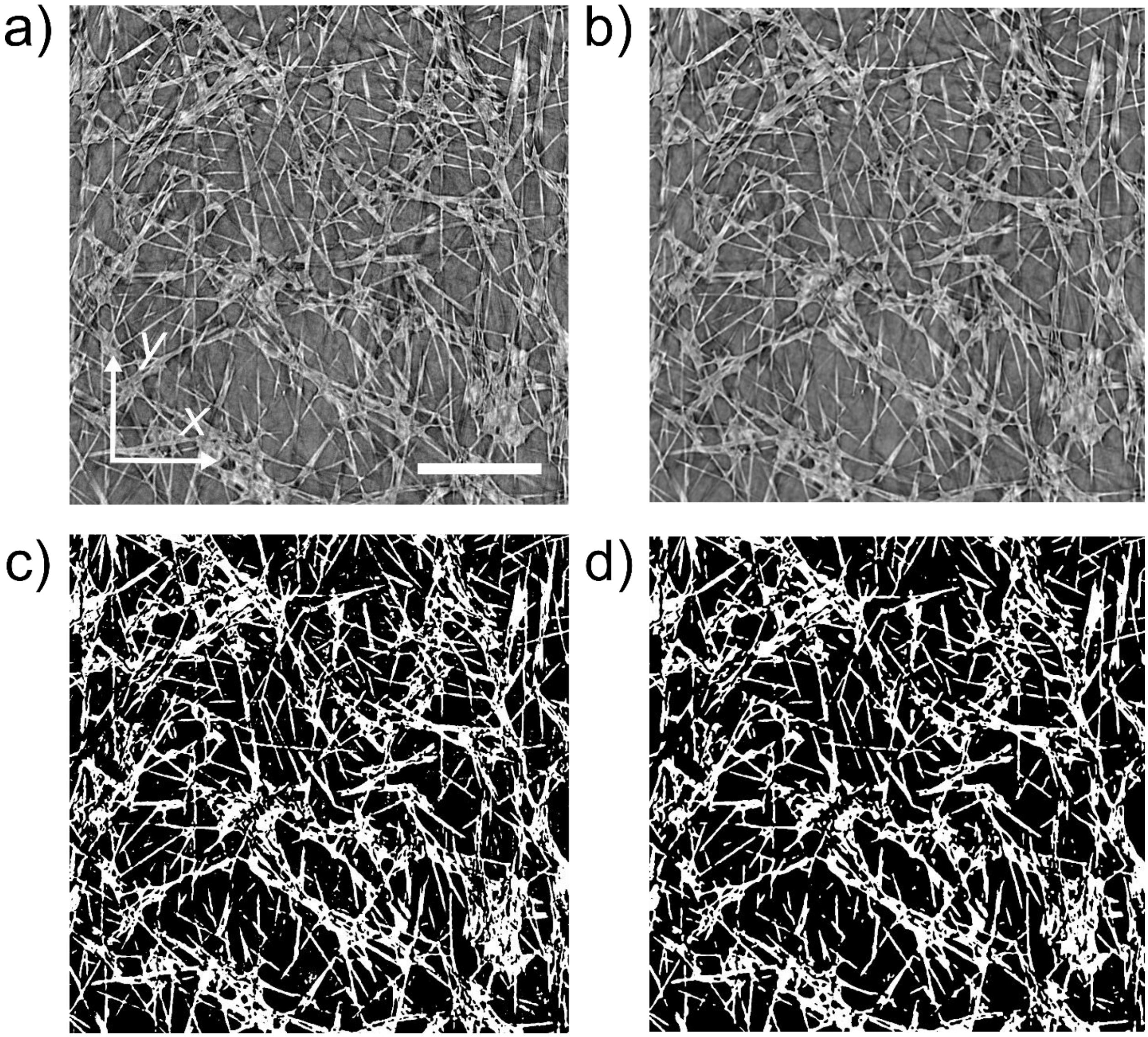


**Figure 3-4**: A 2-D cross-sectional image slice of the cathode GDL at a depth of 45.9 mm from the cathode catalyst layer to showcase the image processing procedure used to calculate porosity: (a) OCV reference image, (b) 3D median filter with 3-pixel radius applied to (a), (c) automatic Otsu threshold applied to b), and (d) outliers less than 3 pixels in radius removed and "despeckle" applied to (c). White scale bar in (a) represents a length of 0.5 mm. Images are taken with a pixel resolution of 2.44 µm.

Thresholding was a necessary step for separating objects of interest from the background in an image. In this case we were interested in isolating the GDL fibres from the void spaces in the images. Otsu's threshold is a popular automatic image thresholding technique for images with bimodal histograms (histograms with two distinct peaks) [68], [69] and was selected in this case for its simplicity and effectiveness [70-72] (Figure 3-4c). In Otsu's method, each pixel is assigned to one of two classes, background or foreground. At a basic level, the threshold produced by Otsu's method is determined by either minimizing intra-class intensity variance or maximizing inter-class variance [73]. After thresholding, further image processing was necessary as some noise was still present in the form of random outliers in the image which did not correspond to fibres. To filter this noise, another automatic 3x3 median filter called "despeckle" in Fiji was applied, followed by a process to remove outliers based on a pixel radius threshold (Figure 3-4d).

The result of the above processing was an 8-bit binarized image stack with fibres represented by a pixel intensity of 255 and void space represented by a pixel intensity of 0. This image stack was then imported into Dragonfly for the purpose of creating a pore network of the GDL, a process which will be described in Chapters 4 and 5.

# Chapter 4 – *Distinction and* relationship between local and pore-scale saturation in fuel cell gas diffusion layers clarified via *high-speed operando tomography*

## 4.1 Introduction

The cathode gas diffusion layer (GDL), a heterogeneous structure necessary for the even distribution of reactants to the catalyst layer (CL) and for the efficient drainage of product water, is often an area of interest when it comes to improving polymer electrolyte membrane (PEM) fuel cell performance [74]. Excess water production at high current density operation can cause flooding in the GDL which impedes reactant gas transport to reaction sites at the CL, especially in the channel region [19], [75], [76]. This results in major mass transport losses and a degradation in cell performance. Recently, an interest has been generated on the topic of partially filled pores. Shrestha et al. used synchrotron X-ray computed tomography (CT) to study 3-dimensional (3-D) pore-scale liquid water distributions in a PEM fuel cell operating at low current density and found that water invasion only partially filled certain pores and suggested that mixed wettability in pores due to heterogeneous polytetrafluoroethylene (PTFE) distribution in the GDL impact the phenomena of partially filled pores [77]. Wiesner et al. introduced new mixed wettability algorithms to predict mixed wetting behaviour of PTFE coated GDLs and proposed that partial pore filling can occur due to differences in contact angles on adjacent walls of a single pore which influence the capillary pressure of the pore voxel [78]. While these studies provide an informative introduction to the partial occupation of water in GDL pores, much remains to be understood about the causation and implications of partially filled pores. Understanding the way in which water occupies the pores and impedes reactant gas pathways in the GDL is critical to improving the performance and durability of PEM fuel cells, as it can help inform the design of GDL materials to balance membrane hydration and water retention in the cathode.

In this chapter, we showcase a new PEM fuel cell design for imaging the cathode GDL using synchrotron X-ray CT. We present *operando* synchrotron X-ray CT images visualizing water distributions in 4-dimensional (4-D) at the pore scale. With our images, we conduct a pore-scale analysis of water at different current density steps with a focus on individual pore saturation, where we define pore saturation to be the ratio of liquid water in a saturated pore to the void space within the pore when empty. We distinguish this from the definition of local saturation, which refers to the ratio of liquid water in the GDL to the void space in the GDL. With these results, we can help improve the accuracy of computational models in the prediction of liquid and gas transport through the cathode GDL. Additionally, we also provide considerations for the design of new materials to mitigate mass transport losses in PEM fuel cells to enable their use for high current density applications.

## 4.2 Methods

In Chapter 3, we detailed the hardware and imaging setup used to capture *operando* X-ray CT images of the PEM fuel cell cathode GDL in order to resolve 3-D water distributions. In this section, we outline the experimental operating conditions and procedure used in this chapter in Section 4.2.1. We then provide the imaging procedure used to capture our 2-dimensional (2-D) X-ray CT image stacks in Section 4.2.2. The methodology presented in Chapter 3 was then used to convert the 2-D image stacks into 3-D volumes of the GDL materials, isolate liquid water in the GDL at constant current densities through image subtraction, and segment the different materials in the GDL. We also outline the procedure for determining local and pore saturation through the development of a pore network based on a dry reference image of the GDL operating at OCV conditions.

### 4.2.1 Experimental operating conditions

The cell temperature was held constant at 60 °C via heated water circulation. Inlet gases (both hydrogen and air) were humidified at 57.7 °C, corresponding to a symmetrical relative humidity of 90%. A back pressure of 100 kPa was applied to the anode and cathode, and hydrogen and air were supplied to the anode and the cathode (in counterflow configuration) at 0.375 slpm each. Due to the small active area of the cell, the balanced flow rate (0.375 slpm) was selected to ensure that the cell could sustain high current densities while not completely drying out the membrane. High current density performance was prioritized to allow us to observe high amounts of water accumulation in the GDL, as our objective is to observe water distributions and dynamic behaviour at the pore scale.

Experiments were performed using a Scribner 850e Fuel Cell Test Station (Scribner, USA). Humidified gases were first flowed through the heated cell without current load for 5 minutes to obtain a stabilized OCV reading. Constant current load was then applied in denominations of 0.25 $A \cdot cm^{-2}$ over a range beginning at 0.25 $A \cdot cm^{-2}$ and ending at cell failure (inability of cell to reach the target current density), which was ~2.0 $A \cdot cm^{-2}$ for the operating conditions stated above. Each current load was applied to the cell for 15 minutes to reach a stable voltage reading.

### 4.2.2 Imaging schedule

Before conducting experiments, flat field images of the beam were taken with the sample absent to correct for bright spots in the beam in image reconstruction. Dark frames were also collected with the beam off to correct for camera noise in reconstruction. The protocol for image collection across the experiment began with taking a dry reference scan of the active area at stabilized OCV. After 12 minutes of constant current load application, one scan was taken to capture the steady state distribution of water at the intended current load. This process was repeated for each change in current load throughout the experiment. At the end of the experiment, a dry reference scan at OCV was taken again.

### 4.2.3 Determining local and pore saturation

To obtain the local saturation of the GDL, we first segmented a dry reference image of the GDL into the fibre structure and void space. We then segmented the water from the subtracted image, such as in Figure 3-3d, and divided the water volume by the void volume:

$$S_L = \frac{V_\mathrm{w}}{V_v} \tag{4.1}$$

where *S* is local saturation, $V_w$ is the volume of water and $V_v$ is the volume of void space.

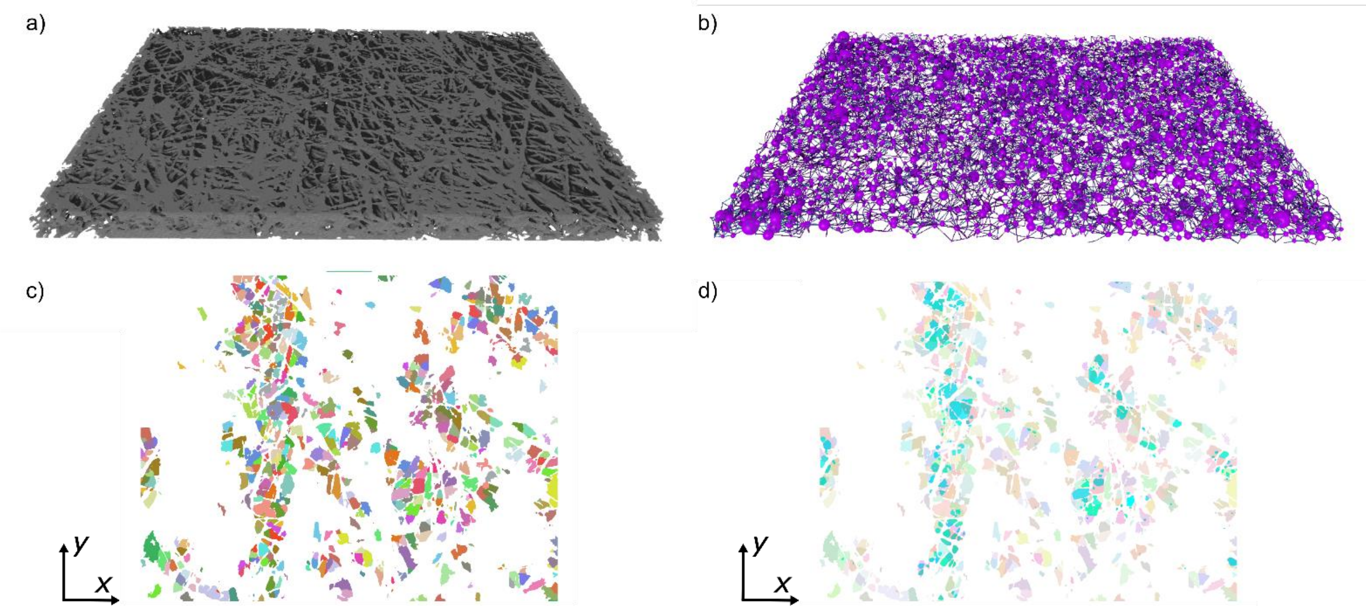


**Figure 4-1**: Steps to obtain isolated pores for analysis: (a) Segmented fibre structure, (b) Pore network model created from the fibre structure in (a) using OpenPNM, (c) Pores with any volume of water present (each colour corresponds to a different pore), created by intersecting segmented water with the pore network model in (b), and (d) The isolated water (cyan) contained within the pores in (c) (remaining colours).

To isolate the pores and the water within them for our pore-scale analyses, OpenPNM was utilized to create a pore network of the GDL [79]. To create this PNM, we first segmented the fibres from a dry reference image of the GDL (Figure 4-1a). We then used the OpenPNM feature under Pore Network Modelling in Dragonfly (ORS Research Systems) to create the pore network from the segmented fibres. The default settings (Sigma value = 0.4, R max = 4, edge tolerance = 0.10%, phase index = 0) were used to create the resulting network in Figure 4-1b. Next, we isolated the pores that contained water by intersecting the segmented water with the pore network, selecting the “Keep Intersected” option. The result was the set (multi-region of interest (ROI)) of pores in the network where water is present (wet” pores) (Figure 4-1c). To get average pore saturation,

$S_{P,avg}$, the volume of the isolated water (cyan in Figure 4-1d), $V_W$, was divided by the volume of the "wet" pores (all colours in Figure 8c), $V_{P,W}$:

$$S_{P,avg} = \frac{V_W}{V_{P,W}} \tag{4.2}$$

Using the scalar generator menu item, we extracted label, volume, and centre of mass index for each of the empty "wet" pores. To obtain information about the water occupying these pores when saturated, we created a new multi-ROI by subtracting the isolated water from the "wet" pores. The resulting multi-ROI was a collection of all the "wet" pores minus the water occupying each pore; that is, each pore contained only the empty space in the pore left over after the invasion of water. Using the scalar generator again, we extracted the pore label and volume of the pores for the new multi-ROI representing the empty volume of each of the pores minus the water contained in them.

To calculate the liquid water saturation of each pore with the data extracted from the new multi-ROI, we used the following formula:

$$S_P = \frac{V_{P,E} - V_{P,F}}{V_{P,E}} \tag{4.3}$$

Where $S_P$ is the liquid water saturation of the pore, $V_{P,E}$ is the volume of the empty pore, and $V_{P,F}$ is the volume of the empty space remaining in the pore after water invasion.

## 4.3 Results and Discussion

In this section, the constant-current electrochemical performance of the cell and the results of operando imaging are discussed. The electrochemical performance of the cell is first reported alongside *operando* images of the cathode GDL (Section 4.3.1). We then discuss the existence of partially filled pores in water distributions and their relationship to local saturation, which are first quantified and visualized through pore-scale analyses in a spatial context (Section 4.3.2) and then in a temporal context (Section 4.3.3). Finally, we demonstrate the implications of partially filled pores on oxygen transport in the GDL and the impact that neglecting this finding has on pore-scale modelling (Section 4.3.4).

### 4.3.1 Electrochemical performance and operando imaging

Benchmark testing of the CT cell indicated comparable performance to lab-scale fuel cells found in previous studies [80], showing a distinct mass transport dominant region where losses are no longer linear after 1.0 $A{\cdot}cm^{-2}$ (Figure 4-2a). Water accumulation in the cathode GDL gradually impeded performance as current density increased, reaching a limit of ~2 $A{\cdot}cm^{-2}$. At 2.0 $A{\cdot}cm^{-2}$, large amounts of water accumulated under the land regions of the GDL (Figure 4-2c), as expected in carbon paper GDLs based on previous studies [81], [82]. Despite adequate performance, the OCV was relatively low (0.81 V, Figure 4-2a), which was likely caused by partial membrane dehydration due to high gas flow rates and prior tests at lower humidity.

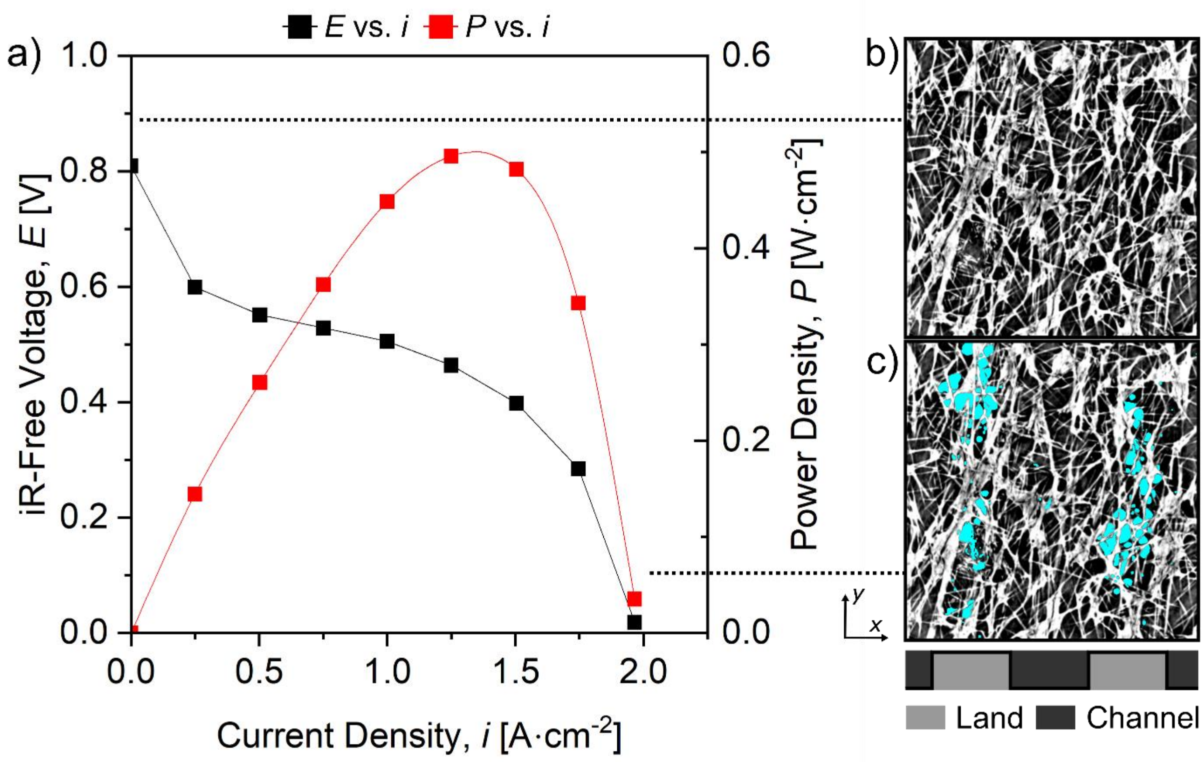


**Figure 4-2**: a) Polarization and power density curves for Toray 060 10% wt. operated at 90% inlet relative humidity (RH) with b) dry reference image slice at OCV and c) water droplet distribution at same slice close to limiting current (2.0 A·cm$^{-2}$). OCV is 0.81 V and power density peaks at about 1.25 A·cm$^{-2}$. The polarization curve demonstrates high activation losses by the large drop from OCV to the first current step of 0.25 A·cm$^{-2}$. However, we shift our focus to the mass transport region as we are interested in water distributions within the GDL and their contributions to performance loss. A cross-sectional through-plane image of the GDL at a depth of 43.9 µm from the catalyst layer is shown in (b) operating at OCV and in (c) operating close to limiting current at 2.0 A·cm$^{-2}$ showing signs of liquid water saturation.

### 4.3.2 Pore saturation increases with local saturation

In the following sections, we discuss how average pore saturation tends to follow changes in local water saturation content in the GDL (e.g. higher pore saturation corresponds to higher local saturation). This is true in both the through-plane and in-plane directions. Additionally, we discuss the higher, heterogeneous accumulation of water under the land regions of the GDL than under the channels, and the resulting low pore saturation under the channel regions.

#### 4.3.2.1 Pores are more saturated at the CL-GDL interface than at the GDL-FF interface

The 3-D images collected in this study enable us to view water distributions in the GDL at the pore scale. We can visualize individual pores in multiple planes of view, where a single pore is highlighted within the fibrous structure of the GDL such as in Figure 4-3. To represent the mean pore saturation at the CL-GDL interface, a partially filled pore located at the CL-GDL interface with a similar saturation to the mean is visualized (Figure 4-3). In Figure 4-3, water (cyan) is separated from the empty pore space (yellow). The water droplet is mostly spherical and occupies the more central region of the pore where the diameter is wider and less constricted than in crevices. Partial pore filling was also observed by Shrestha et al. [77], who had suggested that this phenomenon is due to capillary barriers imposed by narrow constrictions in pore morphology or mixed wettability conditions in GDL fibers and channel boundaries.

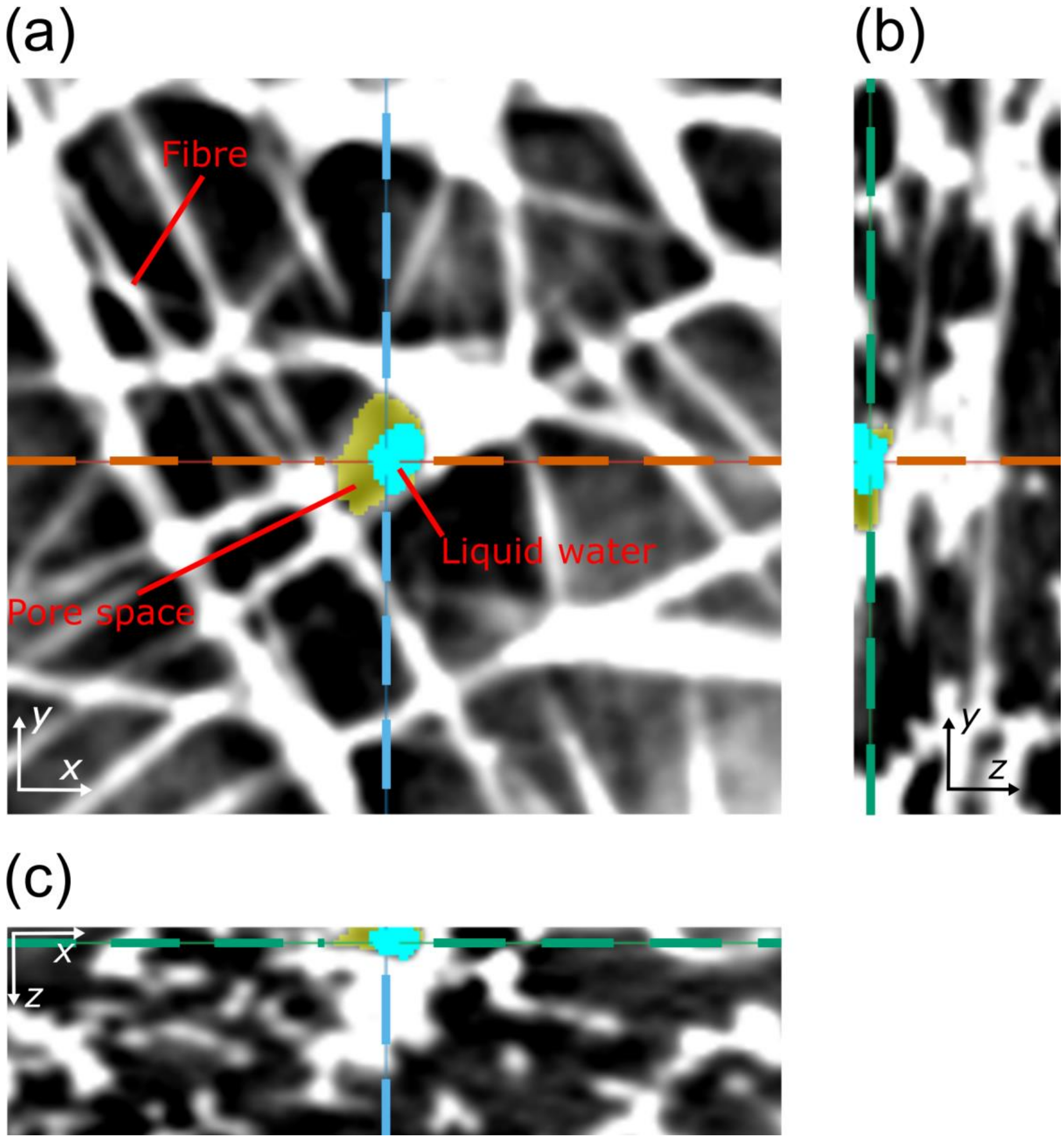


**Figure 4-3**: A single pore located at the CL-GDL interface is visualized from the i) *xy* plane, ii) *yz* plane, and iii) *xz* planes. The pore is only partially filled with a similar saturation to that of the mean at the CL-GDL interface (43.7%), where water (cyan) can be clearly separated from the empty pore space (yellow).

In the through-plane direction, water accumulation throughout the GDL is observed to be highest at the CL-GDL interface and gradually decreases until a peak in concentration right before the

GDL-FF interface (Figure 4-4). Water accumulation at the CL-GDL interface is highest because it is the source of water production in the cell. Conversely, high water saturation also occurs at the GDL-FF interface under the lands due to condensation of water vapour caused by thermal gradients and contact with the bipolar plates which provides a cooling effect. Thermal gradients emerge as reactions generate heat at the catalyst layer. As water travels towards the bipolar plates, condensation occurs due to the lower temperatures as well as with contact with the cooler bipolar plates. When comparing pore saturation to local saturation at the same through-plane depth, we find that pore saturation trends follow those of the local saturation.

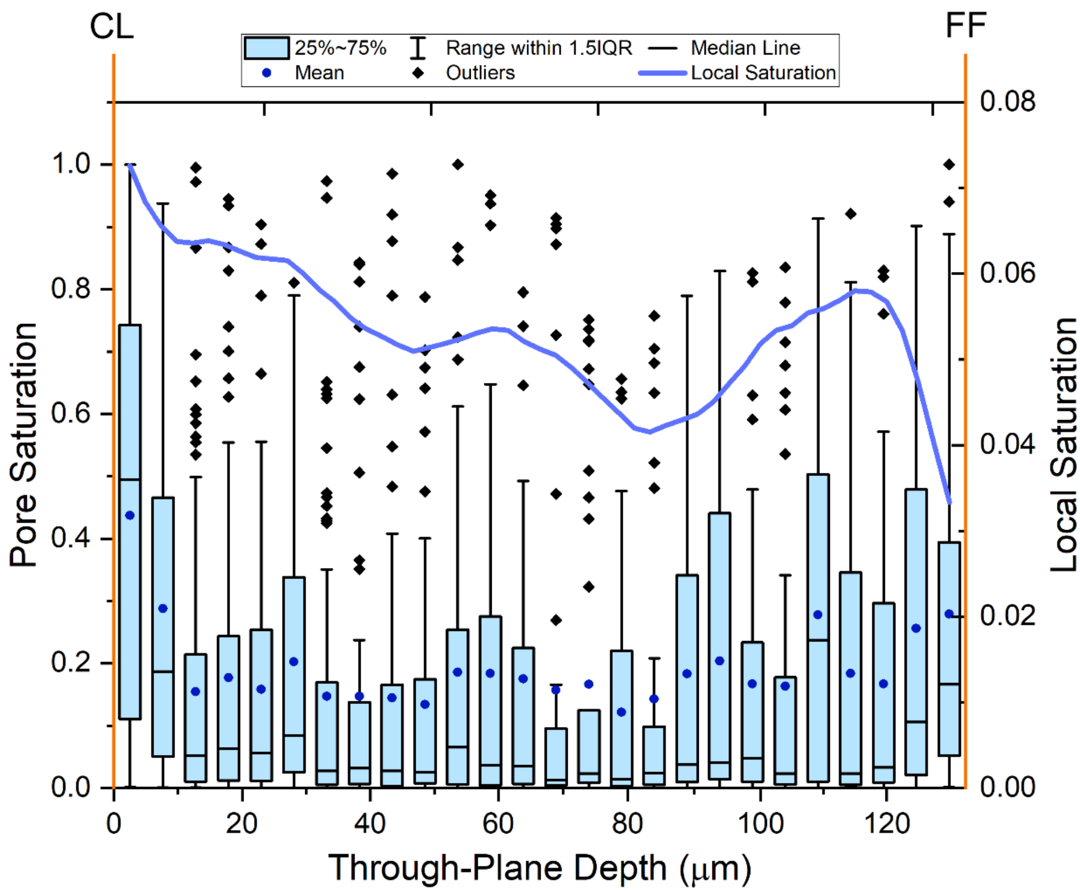


**Figure 4-4**: Pore water saturation (light blue) and local water saturation (dark blue) in the GDL at 2.0 A·cm$^{-2}$ in the through-plane (+Z) direction is described simultaneously where there is a large range of pore saturation points at each depth, but averages and ranges follow the local saturation curve at major points of interest – primarily the peaks and troughs. Local saturation is the highest at the catalyst layer-GDL interface and slowly decreases until there is a peak in saturation close to the flow field-GDL interface. Pore saturation also follows this pattern.

#### 4.3.2.2 Local and pore saturation is higher under the land regions

Liquid water tends to accumulate significantly more under the land regions of the GDL than under the channel regions (86.0% under lands, 14.0% under channels) and that similarly, pores are more saturated under the lands than under the channels on average (19.3% under lands, 11.3% under channels) (Figure 4-5). As observed in previous studies [81-83], we expected to see more water under the land regions of the GDL; however, our observation of higher pore saturation under the lands further corroborates what appears to be a strong relationship between local saturation and pore saturation.

In addition to low local saturation in the channel regions, pore diameter influenced by GDL compression may contribute to low pore saturation in the channel regions. The physical barrier of the lands at the GDL-FF interface leads to greater compression of the GDL under the lands. Previous studies have shown that higher compressive loads reduce pore diameter and porosity in the GDL [84], [85], consistent with our observations of smaller average pore diameters under the lands compared to the channels (Table in Figure 4-5). Since larger pores retain water less effectively, water tends to accumulate more easily in the smaller pores under the lands, resulting in higher pore saturation in these regions.

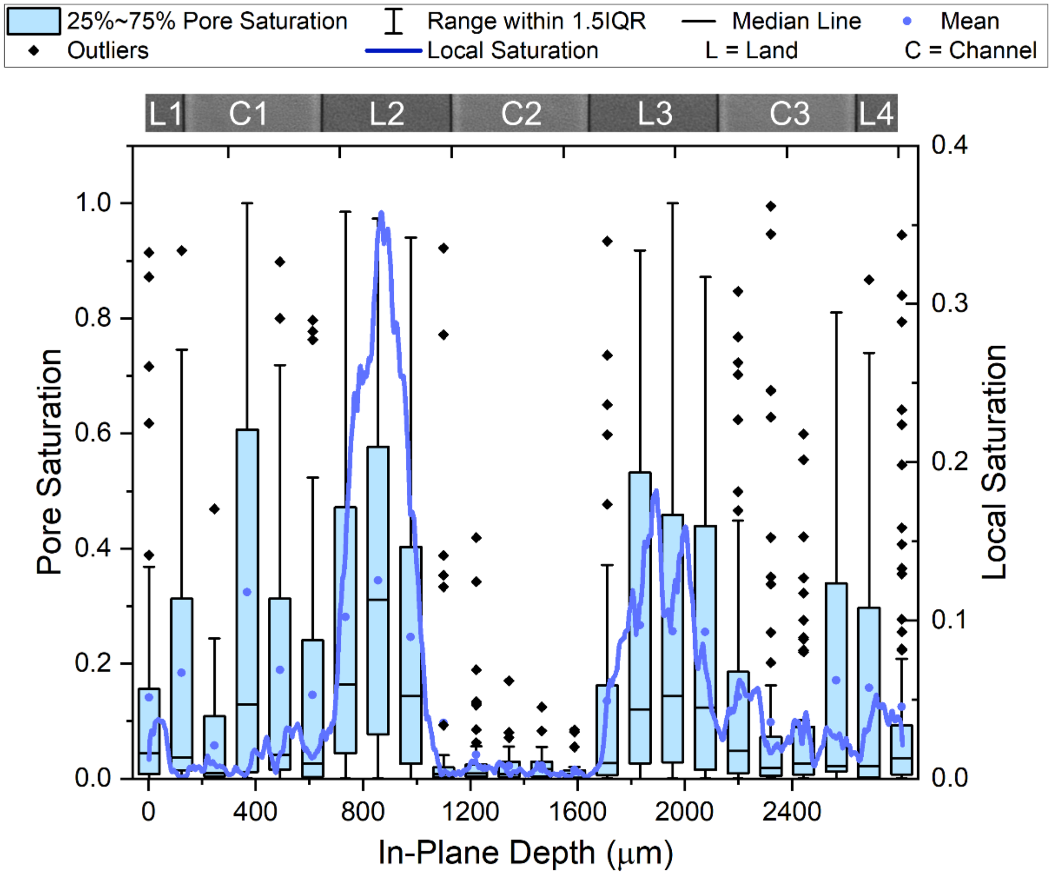


| Parameter | L1 | C1 | L2 | C2 | L3 | C3 | L4 |
|---|---|---|---|---|---|---|---|
| Average pore diameter (μm) | 40.7 | 42.8 | 41.5 | 43.3 | 41.3 | 44.3 | 39.9 |
| Median pore diameter (μm) | 37.8 | 40.0 | 37.0 | 40.7 | 37.1 | 40.9 | 36.0 |

**Figure 4-5**: Pore water saturation (light blue) and local water saturation (dark blue) in the GDL at 2.0 A·cm$^{-2}$ in the in-plane (+X) direction are described together where the bar at the top of the graph represents the positions of the lands (dark grey) and the channels (light grey) with respect to the x-axis. High local and pore saturation are observed under the land regions of the GDL compared to under the channel regions, which are influenced by reduced pore diameters under the lands. Due to higher local saturation across the in-plane direction than across the through-plane

direction, the y-axis limit in this figure is higher than in Figure 4-4. Mean and median pore diameters for each land and channel region of the GDL are reported in the table below the plot.

### 4.3.3 Evolution of pore and local saturation as a function of current density

The observed trend that pore saturation increases with local saturation is also observed at lower current densities and becomes more prominent with an increase in current density (Figures 13 and 14). At 1.25 $A{\cdot}cm^{-2}$ current density operation, water is only present in the first half of the GDL closest to the CL-GDL interface as water production increases in the CL (Figure 4-6a), but not enough for water to have accumulated in the rest of the GDL. At 1.5 $A{\cdot}cm^{-2}$, significantly more water is present in the GDL at the mid point as well as near the flow field as water production increases and water travels from the CL to the flow field region (Figure 4-6b). At 1.75 $A{\cdot}cm^{-2}$, there is again a significant increase in water in all regions of the GDL, with the highest production of water still at the CL-GDL interface as reactions continuously take place (Figure 4-6c). Moving further away from the CL-GDL interface, local saturation gradually decreases until a peak at the GDL-FF interface caused by the accumulation of water under the land regions of the GDL. This peak increases significantly with current density as does the temperature at CL reaction sites, which can be exacerbating the thermal gradient and increasing humidity in the cathode, creating more favourable conditions for condensation at the GDL-FF interface.

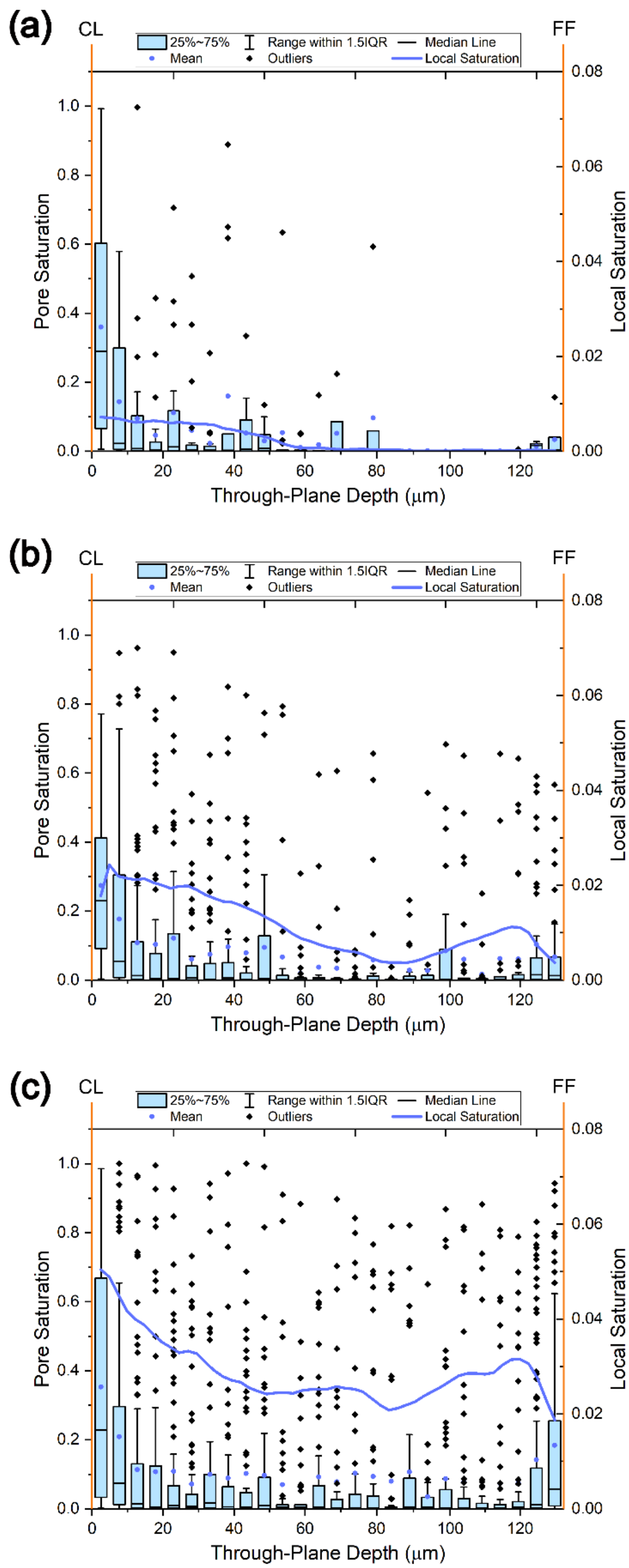
(a)
(b)
(c)
CL
FF
25%~75%
Range within 1.5IQR
Median Line
Mean
Outliers
Local Saturation
Pore Saturation
Local Saturation
Through-Plane Depth (μm)

**Figure 4-6**: Local and pore saturation in the through-plane direction are represented at current densities of (a) 1.25 A·cm$^{-2}$, (b) 1.50 A·cm$^{-2}$, and (c) 1.75 A·cm$^{-2}$. Even at low current densities where there is low water content in the GDL, mean pore saturation levels still tend to follow changes in local saturation.

At 1.25 A·cm$^{-2}$, when there is very little water present in the cathode, average pore saturation under the channel regions of the GDL is negligible while there is some pore filling under the land regions (Figure 4-7a). Local saturation under the lands dramatically increases from 1.25 A·cm$^{-2}$ to 1.50 A·cm$^{-2}$; conversely, pore saturation increases minimally among the pores which were already saturated at the previous current step, while new areas in the GDL that did not previously display saturated pores see a notable increase in pore saturation (Figure 4-7b). From 1.50 A·cm$^{-2}$ to 1.75 A·cm$^{-2}$, local saturation continues to increase as pores become more saturated on the left side, but less saturated on average in some areas on the right side (Figure 4-7c). From 1.75 A·cm$^{-2}$ to 2.00 A·cm$^{-2}$, local saturation almost doubles under the land regions, while the channels generally remain dry. However, pore saturation increases greatly in all regions of the GDL, excluding the middle channel (Figure 4-5). The case in which the local saturation may be higher than the pore saturation could be attributed, for example, to the scenario where there are few large pores that are only partially filled. The minimal increase in pore saturation among existing saturated pores from 1.25 A·cm$^{-2}$ to 1.50 A·cm$^{-2}$ may be explained by mixed wettability conditions within the individual pores, where certain areas of the pores may be more resistant to the invasion of water than surrounding pores which were previously unfavourable to invade. The gradual increase in pore saturation in the channel regions of the GDL from 1.25 A·cm$^{-2}$ to 1.75 A·cm$^{-2}$ is the likely cause for the increase in mass transport losses within this performance region which are represented by the gradual decrease in the polarization curve slope in Figure 9. The higher increase in pore saturation in the channels between 1.75 $A\cdot cm^{-2}$ and 2.00 $A\cdot cm^{-2}$ may also be the cause for the increase in mass transport losses over this period, which is indicated by the steeper decrease in performance compared to the previous current densities. Finally, the gradual increase in mass transport losses over time, despite minimal water content in the channels at lower current densities, suggests that water under the land regions still affects performance, although water under the channels typically has a greater impact [76].

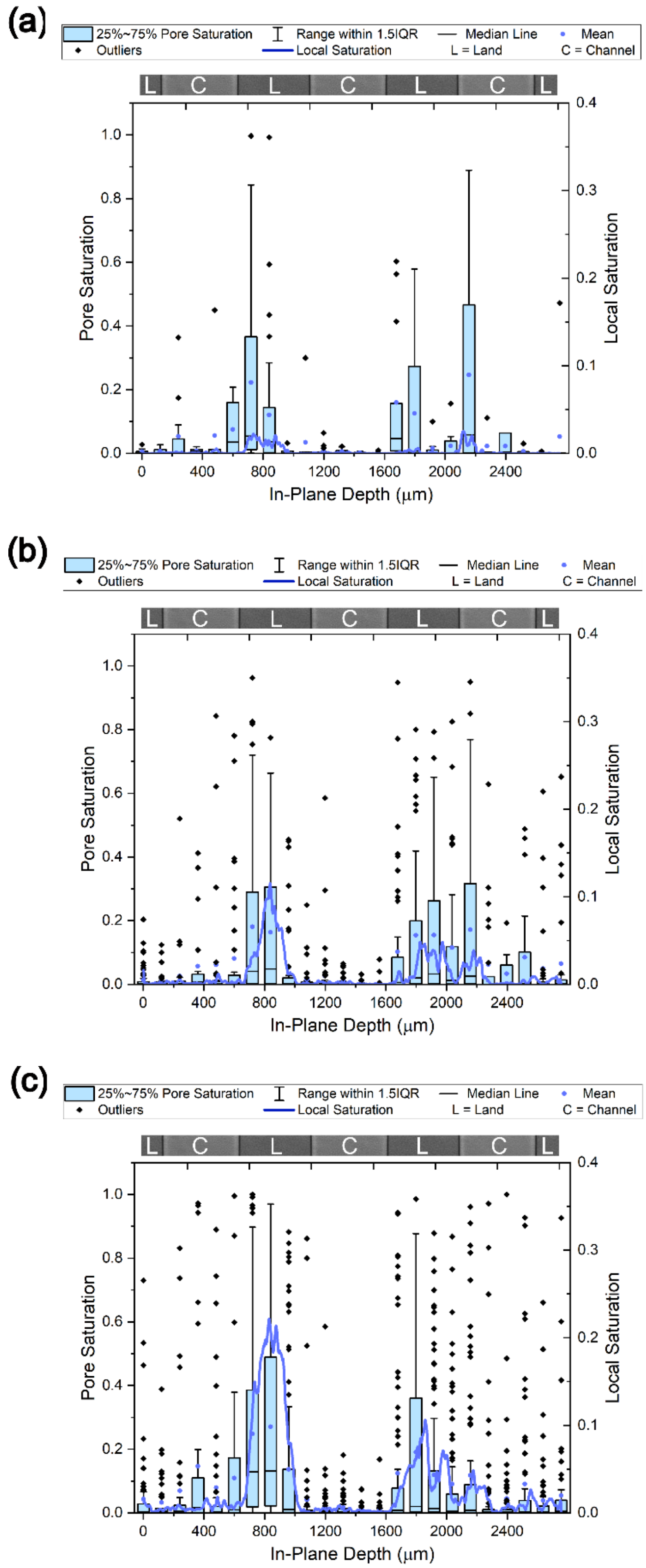
(a)
25%~75% Pore Saturation
Range within 1.5IQR
Median Line
Mean
Outliers
Local Saturation
L = Land
C = Channel
L C L C L C L
Pore Saturation
Local Saturation
In-Plane Depth (μm)
(b)
25%~75% Pore Saturation
Range within 1.5IQR
Median Line
Mean
Outliers
Local Saturation
L = Land
C = Channel
L C L C L C L
Pore Saturation
Local Saturation
In-Plane Depth (μm)
(c)
25%~75% Pore Saturation
Range within 1.5IQR
Median Line
Mean
Outliers
Local Saturation
L = Land
C = Channel
L C L C L C L
Pore Saturation
Local Saturation
In-Plane Depth (μm)

**Figure 4-7**: Local and pore saturation in the in-plane direction are represented at current densities of (a) 1.25 A·cm$^{-2}$, (b) 1.50 A·cm$^{-2}$, and (c) 1.75 A·cm$^{-2}$. Like the pattern observed when current density is close to limiting current, pore saturation closely follows trends in local saturation at lower current densities when water is present. This pattern becomes more pronounced with an increase in current density.

### 4.3.4 Partially saturated pores mean lower oxygen transport resistance than assumed in modelling

We observe that most pores are partially filled rather than fully filled as is usually assumed in numerical modelling of gas flow through saturated GDLs. The influence of pore shape and mixed wettability on pore capillary pressures is likely the cause of partial pore filling. Previous work shows that water preferentially flows through larger pores and throats [86] and is retained more in pores with higher hydrophilicity [87]. Pore shape also causes partial pore filling by influencing capillary pressure within the pore. For example, small crevices at the edges of pores tend to be more hydrophobic due to the presence of PTFE agglomerates, and the combination of size and the likelihood of hydrophobicity in these small crevices increases the capillary pressure needed to overcome for water to invade, leaving water more likely to avoid these spaces. Figure 4-3 demonstrates this phenomenon, where water resides in the open space of the pore rather than filling the crevices at the edges first. In the through-plane direction, hydrophobic and hydrophilic pores may also contribute to differences in pore saturation throughout the thickness of the GDL, aside from the effects of water production at the catalyst layer and water accumulation at the flow field. The mix of hydrophobic and hydrophilic pores may also have an impact on the range in pore saturation in the in-plane direction, although the location of pores with respect to the lands and channels have a more dominant effect due to the difference in GDL compression and thermal gradients between the land regions and the channel regions.

The implication of partially filled pores is that the calculated oxygen transport resistance when assuming fully filled pores is higher than the actual oxygen transport resistance occurring in experimental tests. To quantify the impact that partially filled pores have on gas transport through the cathode compared to the assumption of fully filled pores, we calculated air permeability through the GDL in the through-plane, in-plane, and cross-plane directions. Air permeability through the GDL was calculated for three conditions: dry, fully saturated pores at 2.0 $A \cdot cm^{-2}$, and partially saturated pores at 2.0 $A \cdot cm^{-2}$. For the fully saturated condition, each pore that contained any amount of water in the experimental images was blocked to portray a fully filled pore instead. For the partially filled condition, the experimentally accurate pore saturations were maintained. The results show that compared to the fully saturated condition, permeability was 26.4% higher in the through-plane direction and 50.9% higher in the cross-plane direction with the partially saturated condition. In the in-plane direction, the GDL was impermeable under the fully saturated condition due to water blocking pathways under the lands of the flow field, but the partially filled GDL had a relative permeability of 0.72 to the dry condition. These metrics are available in Table 4-1 below. It is important to note that these permeability calculations were performed for the case where we held the number of pores constant; however, in future, the comparison would be strengthened if we held the overall saturation constant (i.e. the total amount of water within the GDL was the same).

These findings can be used to adjust current methods of modelling saturation in carbon fibre GDLs and will lead to more accurate representations of mass transport and its effect on fuel cell performance.

**Table 4-1**: Comparison of air permeability of fully vs partially saturated pores in the GDL at 2.0 A·cm$^{-2}$ calculated in GeoDict and using the dry GDL as a reference.

| Pore State | Current Density (A cm$^{-2}$) | Through-plane Permeability (z-direction) | | Cross-plane Permeability (y-direction) | | In-plane Permeability (x-direction) | |
|---|---|---|---|---|---|---|---|
| | | Abs. (m$^2$) | Rel. (-) | Abs. (m$^2$) | Rel. (-) | Abs. (m$^2$) | Rel. (-) |
| Dry | 0 | 7.21E-12 | - | 1.12E-11 | - | 8.24E-12 | - |
| Fully saturated | 2.0 | 5.22E-12 | 0.72 | 6.40E-12 | 0.57 | N/A* | - |
| Partially saturated | 2.0 | 6.59E-12 | 0.91 | 9.62E-12 | 0.86 | 5.98E-12 | 0.73 |

*The fully saturated GDL was impermeable in the x-direction due to completely blocked pathways by liquid water under the flow field lands.

## 4.4 Chapter Summary

In this chapter, we utilized synchrotron X-ray CT to visualize liquid water accumulation in the cathode GDL of an operating PEM fuel cell at the pore scale. We define and quantify pore-scale saturation for the first time in fuel cell GDLs and discovered that pores are partially filled rather than completely saturated throughout the GDL. We found that, on average, pore saturation increases with local water saturation. We observed that the local saturation is highest at the CL-GDL interface in the through-plane direction, and therefore results in higher average pore saturation in that region. We also observed higher local saturation under the land regions of the GDL than under the channel regions which correspond to, on average, higher individual pore saturation under the lands. These trends appear at both low and high current density and become increasingly prominent with higher current density. We infer that the combination of pore morphology and mixed wettability at the pore scale influences the overall saturation of a pore at any given time. This includes the favourability of one pore to be filled over an adjacent one, and additionally, this favourability can change over time as a pore becomes more saturated. The existence of partially filled pores leads to a significant underestimation of GDL permeability in modelling which influences the accuracy of these results when compared to the actual water distributions as a result of experimental PEM fuel cell operation. To better improve the accuracy of modelling water transport in GDLs, and ultimately leverage the results to inform better design of GDL materials for enhanced liquid water transport, a more in-depth investigation into pore-scale mixed wettability is recommended.

# Chapter 5 – Identifying relationships between inlet gas relative humidity and liquid water saturation in gas diffusion layers via *operando tomography*

## 5.1 Introduction

Product liquid water in the cathode gas diffusion layer (GDL) can lead to uneven oxygen gas delivery to the catalyst-coated membrane (CCM) which reduces polymer electrolyte membrane (PEM) fuel cell efficiency; therefore, there is significant value in the study of liquid water development and distribution in the cathode GDL. One operating condition that is of major importance is inlet gas relative humidity (RH), which can greatly impact PEM fuel cell performance due to its role in membrane hydration and water formation in the cathode GDL. Extensive studies have been conducted to characterize the influence of inlet RH on PEM fuel cell performance including gas mass transfer resistance [88-90], membrane resistance [88], [90-93] and electrode kinetics [88], [89], [91]. Some studies have even used X-ray computed tomography (CT) to visualize relationships between inlet gas RH and liquid water distributions in the GDL. Eller et al. used X-ray tomographic microscopy (XTM) (high resolution X-ray CT) to show liquid water at different feed gas humidities and current densities, analyzing the distribution of water cluster sizes based on the quantification of local and average saturation [42]. From these results, they defined and quantified categories of water cluster connectivity. Chen et al. also used XTM to visualize and characterize liquid water distributions in the microporous layer (MPL) and GDL substrate as a function of inlet gas RH and current density under humid operating conditions at low temperature (45 °C) [94]. They observed only small amounts of liquid water under the channel regions of the MPL/GDL, except under high current density and high RH conditions. Additionally, they discovered that little to no liquid water was present in the MPL away from the catalyst layer (CL)-MPL interface at lower RH and lower current density, while liquid water was observed only under the land regions at higher RH and current density conditions. While these studies contribute important insight into the impact of RH conditions on water distributions in the GDL, much still stands to be understood about the effect of RH on pore-scale water saturation. This understanding can provide insight for engineers to optimize fuel cell materials and operating strategies to ensure effective hydration of the membrane, minimal flooding and mass transport losses, and enhanced PEM fuel cell durability.

In this study, we examine the impact of symmetrical RH conditions at low temperatures (60 °C) on the liquid water accumulation in the cathode GDL using a small-scale PEM fuel cell. We visualize pore-scale water distributions of the *operando* PEM fuel cell through synchrotron X-ray CT images to determine the effects of inlet RH on liquid water transport and pore saturation, which we define in the previous chapter as the ratio of liquid water to void space in the pore when empty, in the cathode GDL.

## 5.2 Methods

In Chapter 3, we detailed the hardware and imaging setup used to capture *operando* X-ray CT images of the PEM fuel cell cathode GDL in order to resolve 3-dimensional (3-D) water distributions. In this section, we outline the experimental operating conditions and procedure used in this chapter in Section 5.2.1. We then provide the imaging procedure used to capture our 2-dimensional (2-D) X-ray CT image stacks in Section 5.2.2. The methodology presented in Chapter 3 was then used to convert the 2-D image stacks into 3-D volumes of the GDL materials, isolate liquid water in the GDL at constant current densities through image subtraction, and segment the different materials in the GDL. Finally, we provide the comprehensive methodology used to determine local and pore saturation with a pore network model for each of the 3 RH conditions in Section 5.2.3.

### 5.2.1 Experimental operating conditions and procedure

The PEM fuel cell was operated and imaged at 3 symmetrical inlet gas RH conditions: 80% RH, 90% RH, and 100% RH. Symmetrical back pressure of 1 atm was applied at each anode and cathode sides. A reactant gas flow rate of 0.375 slpm was supplied in counterflow configuration to the cell. To maintain a cell temperature of 60 °C, a circulating hot water bath was employed to provide heated de-ionized water to the current collectors adjacent to the graphite flow field plates (Fisherbrand Isotemp 4100). A T-type thermocouple was placed inside the cathode flow field for precise temperature control (Omega Engineering, Inc.). To achieve each relative humidity condition, inlet gases were humidified to temperatures of 55.3 °C (80% RH), 57.7 °C (90% RH), and 60 °C (100% RH) for the corresponding experiment. Experiments were conducted in order of increasing RH, first at 80% RH, then 90% RH, and finally 100% RH.

Each experiment was performed with a Scribner 850e Fuel Cell Test Station (Scribner, USA). In each experiment, humidified gases were first flowed through the heated cell without current load for 5 minutes to obtain a stabilized OCV reading. Constant current load was then applied in denominations of 0.25 $A \cdot cm^{-2}$ over a range beginning at 0.25 $A \cdot cm^{-2}$ and ending at cell failure (inability of cell to reach the target current density), which was 2.25 $A \cdot cm^{-2}$ for 80% RH, 1.75 $A \cdot cm^{-2}$ for 90% RH, and 1.5 $A \cdot cm^{-2}$ for 100% RH. Each current load was applied to the cell for 15 minutes to reach a stable voltage reading. To ensure all water in the GDL was removed from the previous experiment before dry reference images were obtained for the next experiment, the following purging protocol was employed between each experiment: flow humidified $N_2$ for 3 minutes, flow humidified reactants ($H_2$ and $O_2$) for 3 minutes, flow dry $N_2$ for 2 minutes, then flow dry reactants for 2 minutes. After purging, the inlet gas humidifier temperature was increased to reflect the new RH condition and the experiment was repeated after humidifier temperature stabilized.

### 5.2.2 Imaging schedule

Before conducting experiments, flat field images of the beam were taken with the sample absent to correct for bright spots in the beam in image reconstruction. Dark frames were also collected in the absence of the X-ray beam to correct for camera noise in reconstruction. The protocol for image collection across experiments began with taking a dry reference scan of the active area at stabilized OCV prior to each experiment. After 12 minutes of constant current load application, one scan was taken to capture the steady state distribution of water at the intended current load. This process was repeated for each change in current load throughout the experiment. At the end of the experiment, the purging protocol was implemented and a dry reference scan at OCV was taken again. This imaging protocol was repeated for each RH condition.

### 5.2.3 Determining local and pore saturation

To obtain local and pore-scale liquid water saturation data, Dragonfly's pore network modelling (PNM) tool was used. The tool utilizes the OpenPNM package developed by Gostick et. al [95]. To create the pore network model, we first segmented the GDL fibres from the void space in the dry reference image. To segment the fibres, Otsu's threshold, a popular automatic image thresholding technique, was applied to the dry reference image [96]. The result was an 8-bit binary image where the isolated fibres were assigned a pixel intensity value of 255 and the void space was assigned a pixel intensity value of 0. The segmented fibres were used as the boundary for the pores, and then the PNM was developed using the default settings (Phase index = 0, Sigma = 0.4, R max = 4, Edge tolerance = 0.10%). The resulting PNM was a list of 6,478 empty pores with information including their label, volume, equivalent diameter, and centre of mass location index.

To calculate the saturation of individual pores, we first isolated the pores that contained water in the scans acquired at a steady current density. In this study, we focused on the results at 1.75 $A{\cdot}cm^{-2}$ since it was the highest current density shared by all 3 RH conditions, and we wanted to investigate the GDL at highly saturated conditions. To isolate the pores containing water at 1.75 $A{\cdot}cm^{-2}$, we used the Boolean operation "Keep Intersected" in Dragonfly between the PNM and the isolated water extracted from each of the subtracted saturated images at 80% RH, 90% RH, and 100% RH. This process resulted in one set (multi-region of interest (ROI)) of pores that contained water at 1.75 $A{\cdot}cm^{-2}$ for each RH condition. We then created a union between the 3 new multi-ROIs, and the result was a new PNM consisting of only the pores that contained any volume of water at 1.75 $A{\cdot}cm^{-2}$ at any of the 3 RH conditions (3,867 pores). Using the scalar generator menu item, we extracted label, volume, and centre of mass index for each of the empty pores. To obtain information about the water occupying the pores at each RH condition, we created 3 new multi-ROIs by subtracting the isolated water at each RH condition from the union developed above. The resulting multi-ROI for each RH condition was a collection of all the pores in the union with a subtraction of the water occupying each pore; that is, each pore contained only the void space in the pore remaining after the invasion of water. Using the scalar generator again, we extracted the pore label and volume of the pores for each of the 3 new multi-ROIs representing the empty volume of each of the pores minus the water contained in them at 1.75 $A{\cdot}cm^{-2}$ for each RH condition.

To calculate the liquid water saturation of each pore with the data extracted from each of the multi-ROIs, we used the following formula:

$$S_P = \frac{V_{P,E} - V_{P,F}}{V_{P,E}} \tag{5.1}$$

Where $S_P$ is the liquid water saturation of the pore, $V_{P,E}$ is the volume of the empty pore, and $V_{P,F}$ is the volume of the empty space remaining in the pore after water invasion.

## 5.3 Results and Discussion

In this section, we examine the relationships between the constant-current electrochemical performance of the fuel cell and liquid water accumulation in the cathode GDL, where we resolve both the local and pore saturation of the GDL. We studied the impact of inlet relative humidity on the electrochemical performance of the fuel cell via iR-corrected voltage and power density performance (Section 5.3.1). We then discuss the impact of inlet relative humidity (RH) on the local and pore saturation patterns in the cathode GDL in both the through-plane and in-plane directions (Section 5.3.2). Finally, we discuss the influence of RH on the formation of new transport pathways, and we discuss the impact of this new knowledge on developing water management strategies and water transport models for advancing electrochemical performance (Section 5.3.3).

### 5.3.1 Electrochemical performance

Improvements to the electrochemical performance of the fuel cell are observed as we decrease the RH of the inlet. Specifically, higher current and power densities are reached at lower RH conditions (Figure 5-1). Electrochemical testing was conducted using the same membrane electrode assembly (MEA) for each humidity condition, and performance was evaluated at 80%, 90% and 100% RH (symmetrically applied on the anode and cathode). The iR-corrected polarization curve (Figure 5-1a) shows a decrease in OCV with increasing RH, which we attribute to the membrane degradation from hydration and dehydration cycling that occurred due to the necessary gas purging at the end of each polarization cycle. Our custom fuel cell is unintentionally susceptible to this type of degradation due to its small active area, which is required for CT imaging.

The polarization curves comparing the inlet conditions are shown in Figure 5-1a, and we observe that with increasing RH, the overpotentials increase at each current density (Figure 5-1a). Further, the maximum current density increases with decreasing RH: at 80% RH, the maximum current density is 2.25 $A \cdot cm^{-2}$, at 90% RH the maximum current density reaches 1.75 $A \cdot cm^{-2}$, and at 100% RH the maximum current density only reaches 1.5 $A \cdot cm^{-2}$. As RH decreases, peak power density also increases (27.4% from 100% RH to 80% RH) (Figure 5-1b) and occurs at a higher current density (1.25 $A \cdot cm^{-2}$ for 100% RH and 1.75 $A \cdot cm^{-2}$ for 80% RH). These performance improvements are attributed to the smaller polarization losses at 80% RH in the activation loss dominant region (< 0.25 $A \cdot cm^{-2}$) and mass transport dominant region (> 1.00 $A \cdot cm^{-2}$) of the polarization curve (Figure 5-1a). The mass transport losses are lower as a direct result of the drier conditions at 80% RH, which leads to a decrease in liquid water accumulation in the cathode gas diffusion layer (GDL) and enables enhanced reactant transport to the catalyst layer (CL). Similarly, the lack of liquid water at the CL leads to higher oxygen content at the reaction sites thereby lower activation losses.

a)

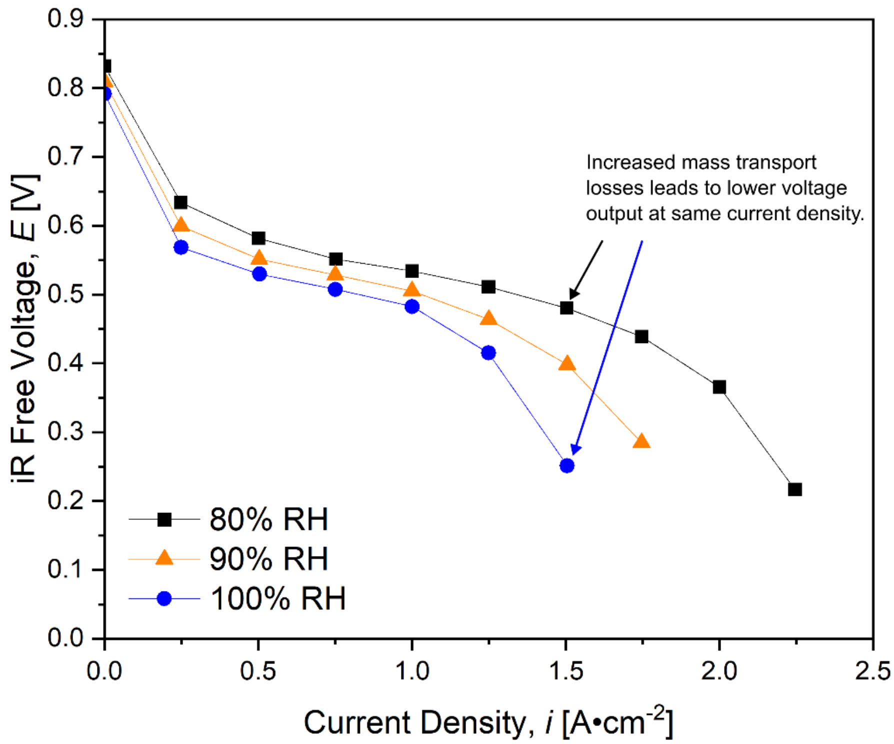

Increased mass transport
losses leads to lower voltage
output at same current density.
80% RH
90% RH
100% RH
iR Free Voltage, $E$ [V]
Current Density, $i$ [A•cm$^{-2}$]
0.0
0.1
0.2
0.3
0.4
0.5
0.6
0.7
0.8
0.9
0.0
0.5
1.0
1.5
2.0
2.5


b)

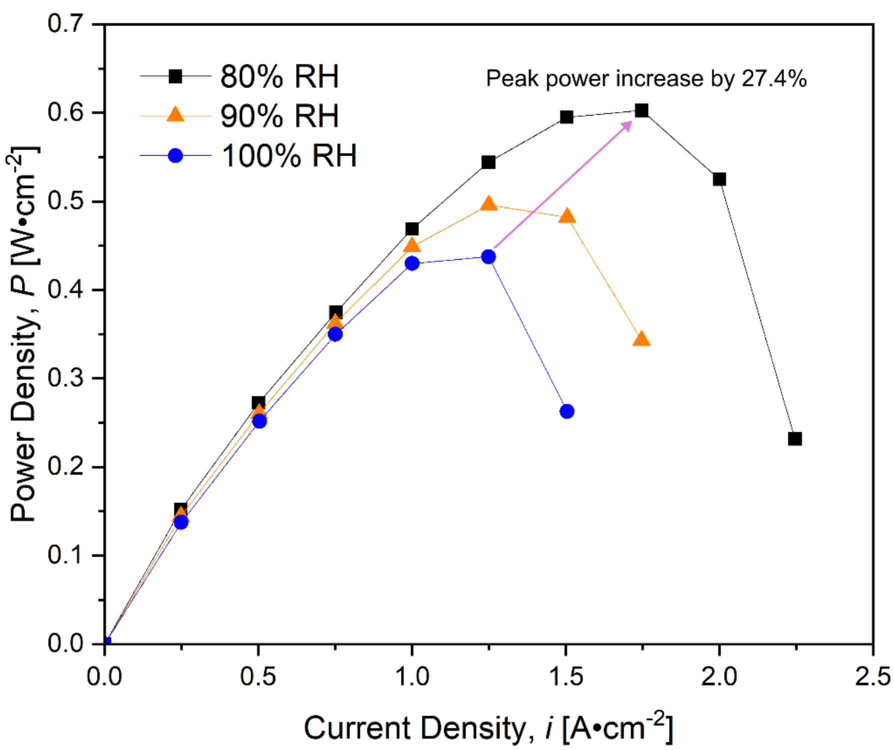

Peak power increase by 27.4%
80% RH
90% RH
100% RH
Power Density, $P$ [W•cm$^{-2}$]
Current Density, $i$ [A•cm$^{-2}$]
0.0
0.1
0.2
0.3
0.4
0.5
0.6
0.7
0.0
0.5
1.0
1.5
2.0
2.5

**Figure 5-1**: Electrochemical performance of the cell for each operating relative humidity showing (a) polarization curve and (b) power density curve. Performance of the cell improves with decreasing inlet relative humidity, as voltage and power output increases, onset of mass transport losses occurs at higher current density, and limiting current is higher as humidity decreases.

### 5.3.2 Local and pore saturation increase with inlet relative humidity

#### 5.3.2.1 Pore saturation is more evenly distributed in the through-plane direction at high RH conditions

In Chapter 4, we observed that in the through-plane direction from the catalyst layer (CL) to the flow field (FF), local saturation is highest at the CL-GDL interface, which corresponds to higher pore saturation at the CL-GDL interface. To investigate the relationship between local and pore saturation at varying RH conditions, we chose to focus on the liquid water distribution at 1.75 $A \cdot cm^{-2}$, since this was the highest current density reached at all RH conditions tested in this study. The local and pore saturations are mapped in the through-plane direction by accounting for all pores in the in-plane direction (across the lands and channels) at each through-plane location for each RH condition (Figure 5-2). We find that local saturations increase with RH, and we identify a correlation between the local and pore saturation, both generally increasing with increasing RH (Figure 5-2). At 80% and 90% RH (Figure 5-2a and 2b), we see that pore saturation follows the local saturation throughout the through-plane direction, increasing and decreasing with respect to the in-plane direction. At the 100% inlet RH condition, pore saturation is more evenly distributed throughout the through-plane compared to the drier RH conditions. The saturation profile also becomes more evenly distributed at 100% RH, but still fluctuates in a similar pattern to the saturation profile at 90% RH.

Compared to the 80% RH condition, at 90% RH, the pore saturation is high at the CL-GDL and GDL-FF interfaces but decreases in these regions as humidity rises to 100% RH. At 100% RH, more significant water accumulation leads to the formation of new pathways, thus facilitating the removal of liquid water to adjacent pores rather than a concentration of liquid water in one location. At the GDL-FF interface, there is the added presence of a physical barrier (the lands) which further encourages liquid water accumulation. This barrier inhibits the further through-plane movement of liquid water, and instead encourages the lateral (in-plane) dispersion of liquid water into adjacent pores. We propose that this behavior likely contributes to the observed increase in average pore saturation in the channel regions when increasing from 90% RH to 100% RH (5-3b and 5-3c). Moreover, since the efficiency of the cell is lower at 100% RH compared to the other RH conditions (indicated by lower voltage at the same current density), more waste heat is generated at 100% RH than at lower RH conditions. This excess heat may lead to higher rates of evaporation and lower pore saturation at the CL-GDL interface.

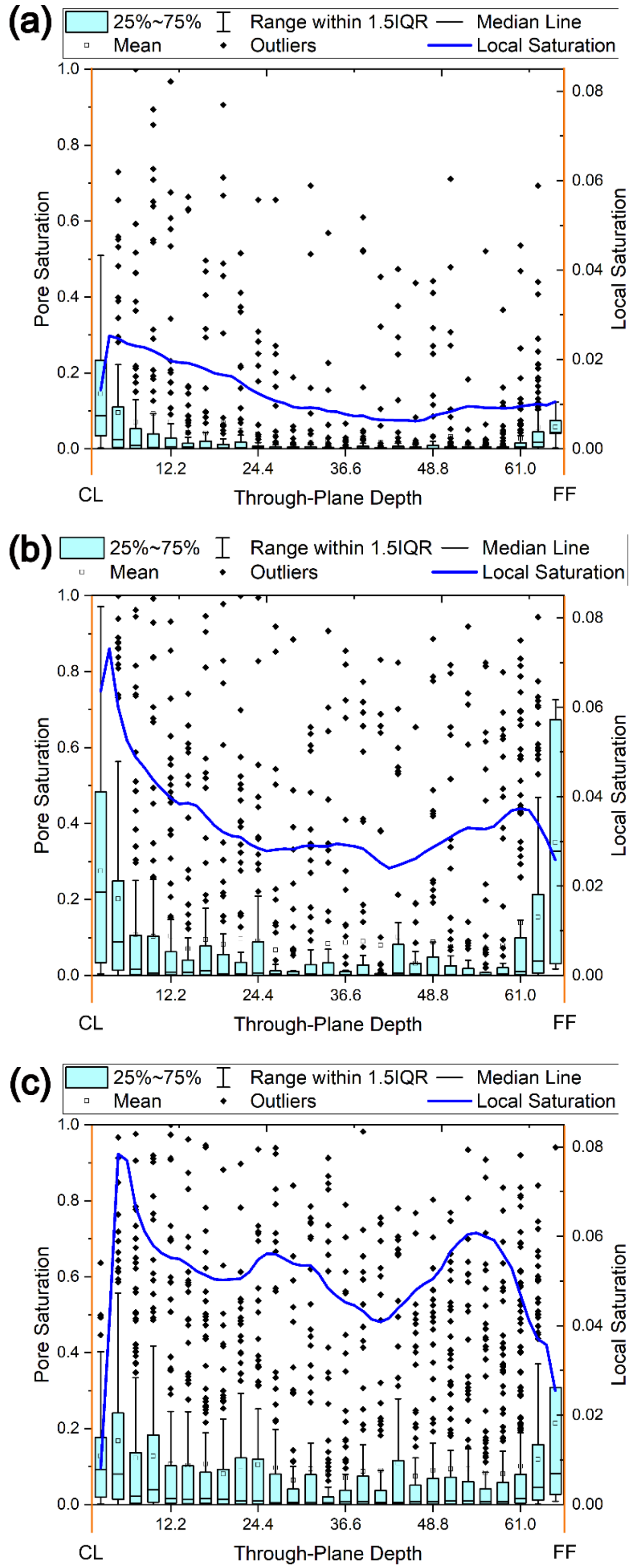

(a)
25%~75%
Range within 1.5IQR
Median Line
Mean
Outliers
Local Saturation
Pore Saturation
Local Saturation
0.0
0.2
0.4
0.6
0.8
1.0
0.00
0.02
0.04
0.06
0.08
12.2
24.4
36.6
48.8
61.0
CL
Through-Plane Depth
FF
(b)
25%~75%
Range within 1.5IQR
Median Line
Mean
Outliers
Local Saturation
Pore Saturation
Local Saturation
CL
Through-Plane Depth
FF
(c)
25%~75%
Range within 1.5IQR
Median Line
Mean
Outliers
Local Saturation
Pore Saturation
Local Saturation
CL
Through-Plane Depth
FF

**Figure 5-2**: Local and pore saturation mapped across through-plane (from catalyst layer to flow field interface) depth at (a) 80% RH, (b) 90% RH, and (c) 100% RH for cell operating at 1.75 $A \cdot cm^{-2}$.

### 5.3.2.2 In-plane local and pore saturation

Here we also present the local and pore saturation in the in-plane direction by accounting for all pores in the through-plane direction at each in-plane location (Figure 5-3). We see again that local and pore saturation increase with RH. Increasing the relative humidity from 80% RH to 90% RH results in significant increases in the local and pore saturations in all GDL regions in the through-plane direction. However, while increasing the relative humidity from 90% RH to 100% RH results in an overall higher saturation profile, at the same time, we observed that the pore saturation decreases in some regions even though adjacent regions become more saturated, particularly under the land regions of the GDL. We attribute these changes in saturation to new transport pathways at 100% RH that are formed adjacent to formerly filled and isolated pores at 90% RH. In some areas, the newly formed transport pathways provided an alternative pathway for liquid water to exit the previously filled pores. We propose that the newly wetted pores (being more hydrophilic than when they were previously dry pores) exhibited lower threshold capillary pressures for invasion, thereby providing new preferential transport pathways for liquid water transport.

(a)

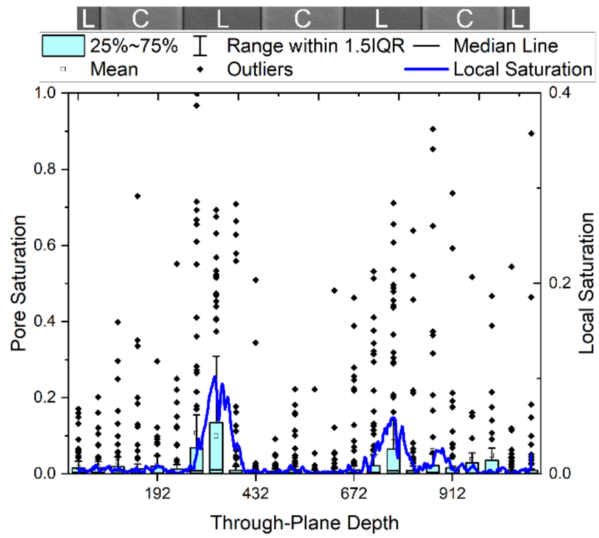
L C L C L C L
25%~75%
Range within 1.5IQR
Median Line
Mean
Outliers
Local Saturation
Pore Saturation
Local Saturation
Through-Plane Depth
192
432
672
912
0.0
0.2
0.4
0.6
0.8
1.0

(b)

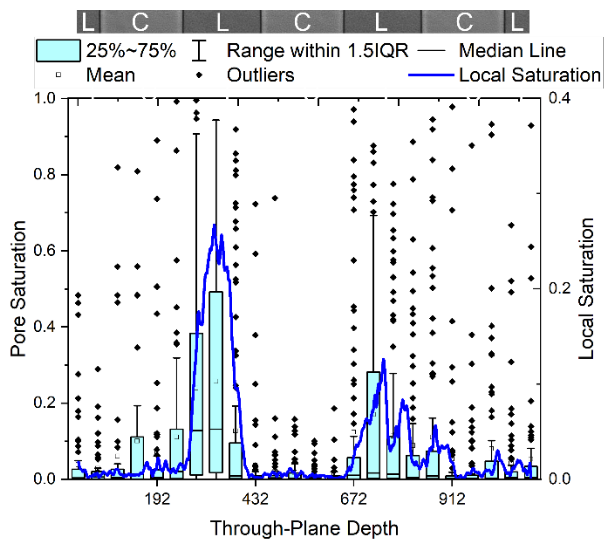
L C L C L C L
25%~75%
Range within 1.5IQR
Median Line
Mean
Outliers
Local Saturation
Pore Saturation
Local Saturation
Through-Plane Depth
192
432
672
912
0.0
0.2
0.4
0.6
0.8
1.0

(c)

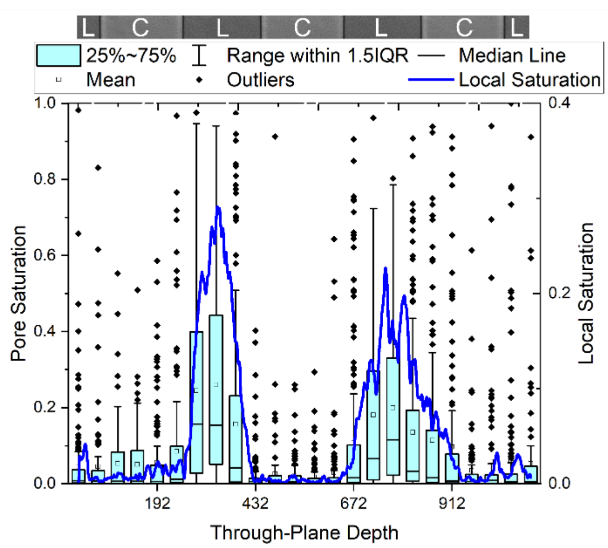
L C L C L C L
25%~75%
Range within 1.5IQR
Median Line
Mean
Outliers
Local Saturation
Pore Saturation
Local Saturation
Through-Plane Depth
192
432
672
912
0.0
0.2
0.4
0.6
0.8
1.0

**Figure 5-3**: Local and pore saturation mapped across in-plane (through flow field regions) depth at (a) 80% RH, (b) 90% RH, and (c) 100% RH.

### 5.3.3 Some areas of pores become less saturated at higher RH

To gain deeper insight into the formation of new liquid water pathways, we analyzed a network of interconnected pores at the pore scale. This network, comprising seven pores, is analyzed in the *xy*, *xz*, and *yz* planes at a selected location to provide an example comprehensive view of the pores and their saturation levels (Figure 5-4). To compare pore saturation as a function of the RH, the network is visualized at four RH conditions: dry (Figure 5-4a), 80% RH (Figure 5-4b), 90% RH (Figure 5-4c), and 100% RH (Figure 5-4d). As we increase the RH, water clusters extend to pores adjacent to the pores initially filled at a lower RH, and the saturations of most pores increase.

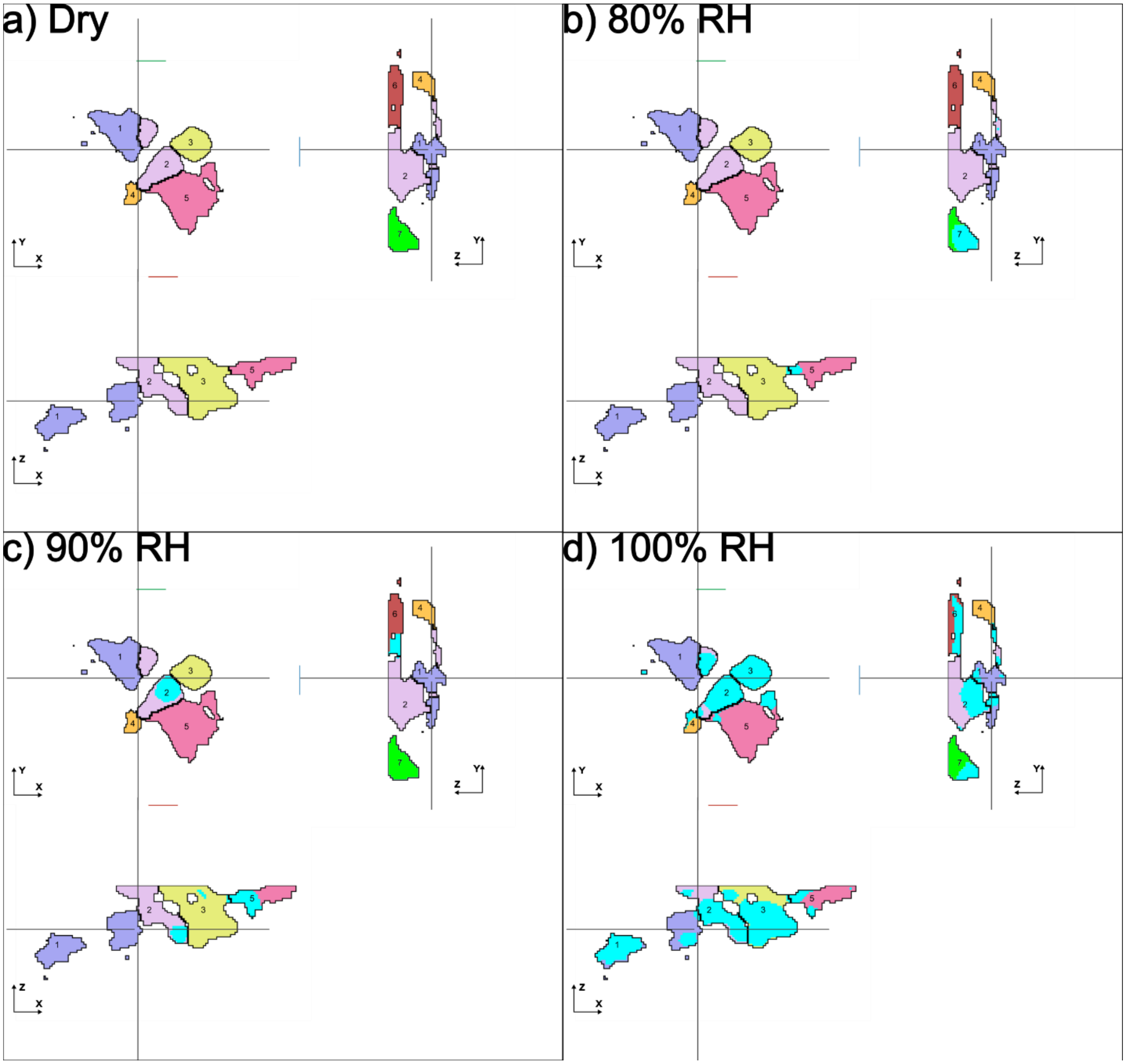


**Figure 5-4**: Cross sectional views (*xy*, *xz*, and *yz* planes) of a representative example, connected cluster of pores in the GDL at (a) dry, (b) 80% RH, (c) 90% RH, and (d) 100% RH conditions. Crosshairs indicate the location of each cross-sectional view. Each pore is numbered and identified by a unique colour, while water is identified by cyan.

To examine the impact of increasing RH on pore filling more closely, we observe the set of pores shown in the *xz* plane alongside the changes in liquid water volume and pore saturation for pores 1, 2, 3, and 5 (Figure 5-5). For each of these pores, saturation and liquid water volume increase with RH. Pores 1-3 exhibit small increases in liquid water volume when increasing the RH from 80% RH to 90% RH, but these pores next exhibit a more significant increase in liquid water volume when increasing from 90% RH to 100% RH. However, pore 5 exhibits a small increase in liquid water volume and pore saturation from 90% RH to 100% RH, despite much more significant increases in liquid water volume at 100% RH in each of the adjacent pores. Revisiting Figure 5-4, we see that some pores, such as pore 7, even exhibit a decrease in saturation when RH conditions increase from 80% RH to 90% RH (Figure 5-4b and 5-4c). We propose that in some pores, such as pore 7, liquid water is removed via newly formed transport pathways. The subsequent increase in saturation from 90% to 100% RH (Figure 5-4c and 5-4d) is attributed to the pressure required to fill pore 7 being less than the pressure required to continue filling the new water pathway formed at 90% RH.

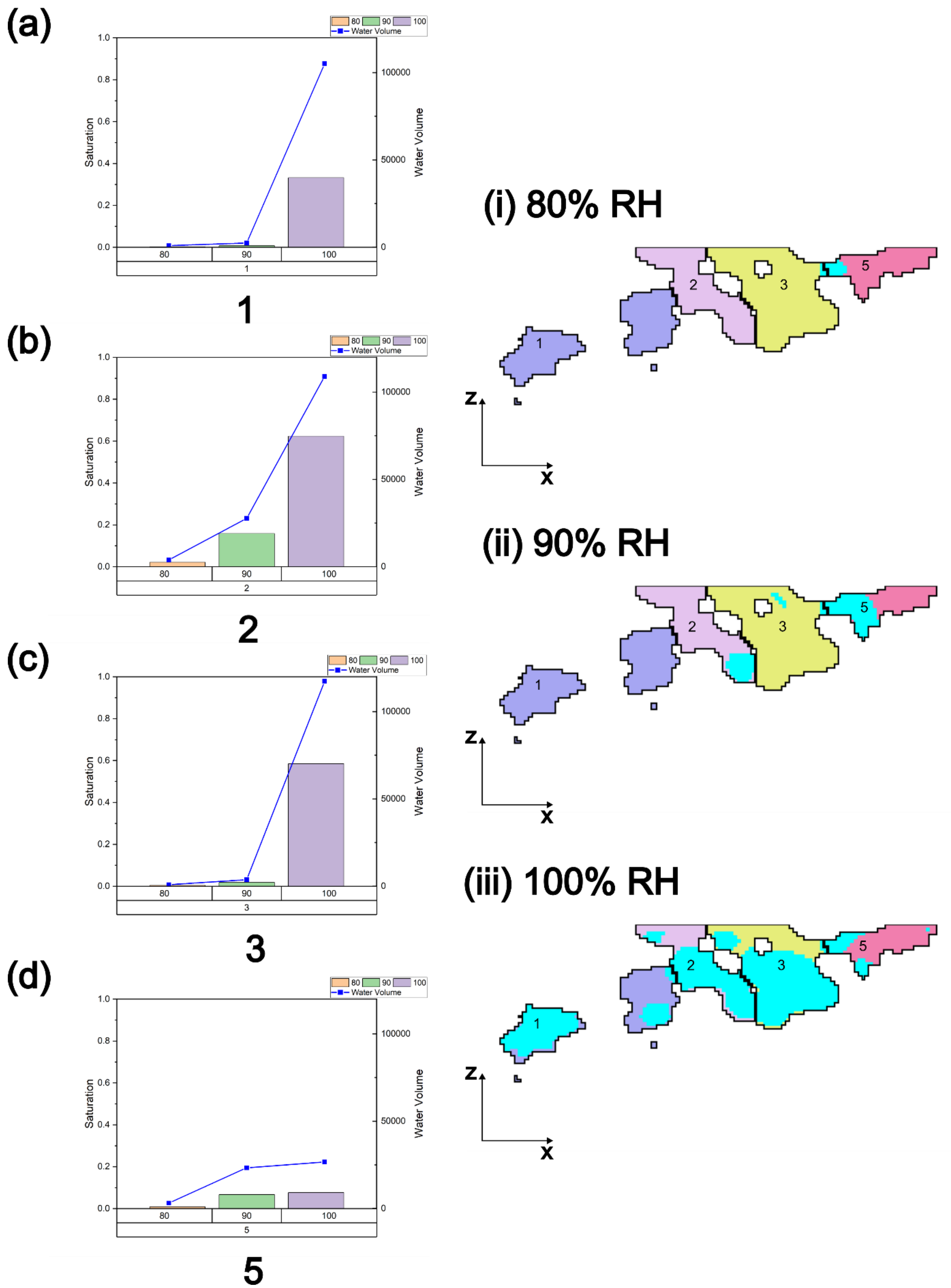

(a)
(b)
(c)
(d)
80
90
100
Water Volume
Saturation
Water Volume
1.0
0.8
0.6
0.4
0.2
0.0
100000
50000
0
1
2
3
5
(i) 80% RH
(ii) 90% RH
(iii) 100% RH
z
x

**Figure 5-5**: Pore saturation and water volume plotted at each relative humidity for (a) Pore 1, (b) Pore 2, (c) Pore 3, and (d) Pore 5 alongside the xz cross-sectional view of the pore cluster for (i) 80% RH, (ii) 90% RH, and (iii) 100% RH. For each pore, saturation increases with relative humidity.

Our observations of preferential pore filling and the formation of new liquid water pathways are supported by a 3-D analysis of the same pore cluster (Figure 5-6), with cross-sections in the *xz* and *yz* planes compared at the following conditions: dry (Figure 5-6a), 80% RH (Figure 5-6b), 90% RH (Figure 5-6c), and 100% RH (Figure 5-6d). Six of the eight pores are visible in Figure 5-6. At 80% RH, the pink (pore 5), yellow (pore 3), and dark purple (pore 7) pores contain liquid water. At 90% RH, liquid water remains in the pink (pore 5) and yellow (pore 3) pores while also extending to adjacent green (pore 8) and pink (pore 5) pores. At 100% RH, liquid water accumulates within the previously filled pores (pores 3, 5, and 7) and additional liquid water invades the remaining light purple pore (pore 2). The consistent retention of liquid water in specific pores across RH levels suggests preferential filling of certain pores (pores 3, 5, and 7), followed by the formation of new pathways in adjacent pores (pores 1, 2, and 8) as local water concentration and adjacent pore wettability increases.

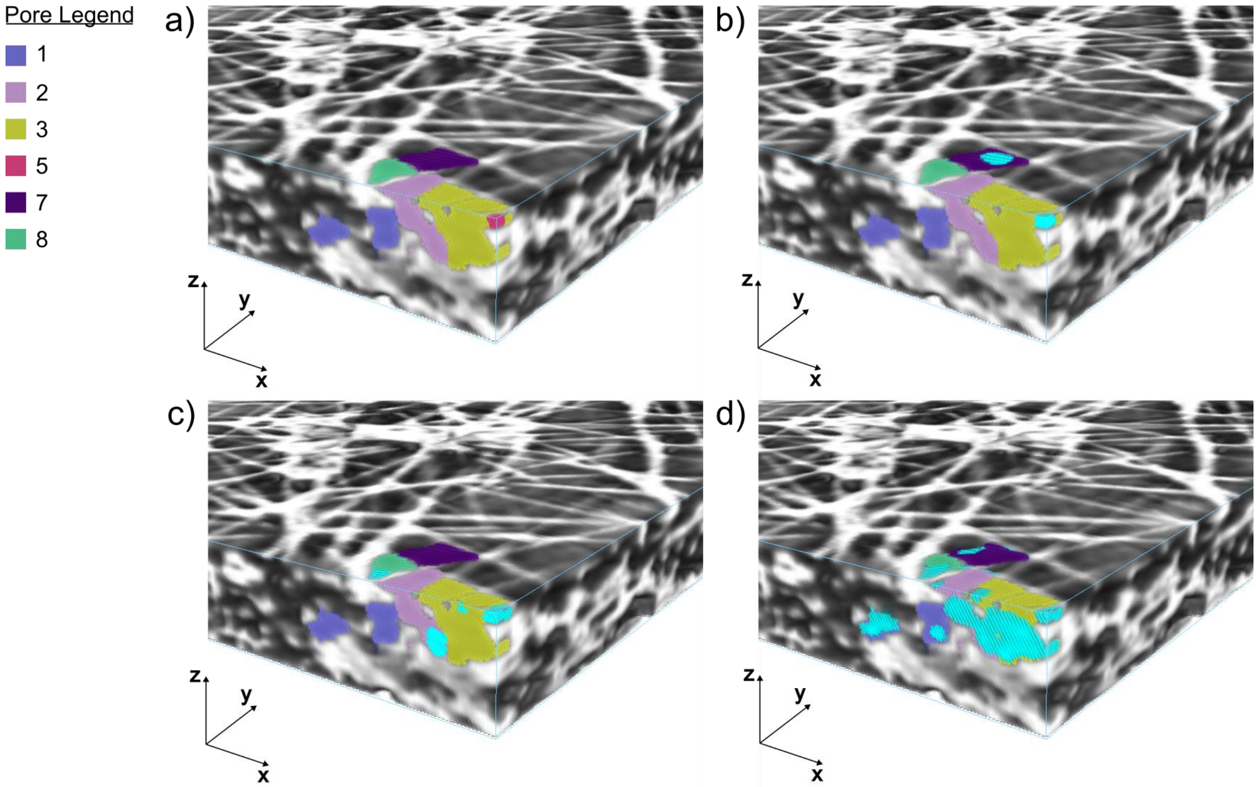


**Figure 5-6**: 3-D view of pore cluster 1 at (a) dry, (b) 80% RH, (c) 90% RH, and (d) 100% RH conditions. Water appears to selectively fill the same pores first (dark purple, yellow) then expand into adjacent pores as local water concentration increases, and initial pores become more filled.

These observations regarding the selective filling of pores and the formation of new water transport pathways have several implications. First, the progressive expansion of water pathways to adjacent pores as RH increases highlights the dynamic nature of liquid water distribution in the GDL. These expanding clusters of transport pathways suggest that water transport is highly sensitive to local saturation conditions and capillary pressures. Next, the observation that the saturation within pore 7 decreases between 80% and 90% RH indicates that newly formed water pathways can act as drainage paths, establishing the redistribution of liquid water within the GDL. The subsequent increase in saturation of pore 7 from 90% RH to 100% RH suggests that pore filling behaviour depends on capillary forces and local pore geometries, as was discussed in Chapter 4. This nonlinear saturation behaviour (decrease in saturation from 80% to 90% RH, increase in saturation from 90% to 100% RH in pore 7) exhibited by some pores shows the complex interactions between capillary forces, pathway formation, and pore connectivity.

These implications provide important insight when it comes to water management strategies and modeling water transport in GDLs under varying RH conditions. In developing effective water management strategies in PEM fuel cells, the dynamic redistribution of water at varying RH conditions must be considered to prevent flooding in the cathode GDL. Additionally, understanding the cause for and characteristics of developed drainage pathways could assist in the optimization of internal GDL structures to enhance water evacuation and maintain gas permeability. Furthermore, developing GDLs with controlled pore size distributions can help tune local capillary pressures to facilitate uniform water distribution, reducing mass transport losses caused by uneven saturation and, consequently, uneven oxygen delivery to the CL. Finally, models of water transport in GDLs must consider nonlinear and dynamic behaviour to accurately predict PEM fuel cell performance under varying RH conditions for enhanced predictive accuracy.

## 5.4 Chapter Summary

In this chapter, we studied the effects of inlet gas RH on local and pore saturation in the cathode GDL by visualizing liquid water at the pore scale with *operando* synchrotron X-ray CT. At an operating temperature of 60 °C, we found that in the 80%-100% RH range, lower RH conditions result in better electrochemical performance with a peak power increase of 27.4% when reducing the RH from 100% to 80%. Additionally, we observed an increase in maximum operating current density with decreasing RH. Analysis of the CT images of the GDL shows that local water saturation increases with RH. When coupling the performance results with our CT images of the local water distribution in the GDL, we propose that mass transport losses are the limiting factor for the performance degradation associated with increasing the RH. While membrane conductivity and performance typically increase with RH at higher temperatures, the decrease in performance that we see with an increase in RH at a more moderate temperature implies that mass transport losses at higher RH are more detrimental to performance than a more hydrated membrane is beneficial. We also found that pore saturation increases with local saturation, and that pores are, on average, more saturated at higher RH conditions due to the higher local saturation. However, we also observe a decrease in pore saturation in some regions throughout the GDL when increasing from 90% RH to 100% RH, which we attribute to the formation of new, adjacent liquid water transport pathways. We propose that as pores in initial pathways become more saturated and water flows into surrounding pores, lower threshold capillary pressures are induced in the surrounding pores due to changes in wettability conditions in the newly wetted pores, which are more hydrophilic than prior to invasion. These new pores then become preferential drainage paths for previously wetted pores, leading to decreasing saturations. Our results suggest that pore filling behaviour depends on local capillary forces and wettability influenced by RH conditions. Furthermore, these findings imply that water transport through the GDL is highly sensitive to local saturation conditions and capillary pressures, and that newly formed water transport pathways can act as drainage paths which redistribute water throughout the GDL. Altogether, our findings demonstrate that the highly complex factors, such as capillary forces, pathway formation, and pore connectivity, influence local pore filling in an operating fuel cell and must be considered in the design of new materials and to improve the accuracy of numerical models.

# Chapter 6 – Conclusions and future work

## 6.1 Summary of findings

The overall objective of this thesis was to add to our understanding of the mechanisms of water transport in the cathode gas diffusion layer (GDL) of a polymer electrolyte membrane (PEM) fuel cell at the pore scale. To accomplish this, X-ray computed tomography (CT) was employed to visualize water in the individual pores of the GDL in 3-dimensions (3-D) in an *operando* fuel cell across varying operating conditions. In Chapter 3, the methodology used to reconstruct and segment the CT images in order to isolate the product liquid water generated by fuel cell operation was explained. In the methodology sections of Chapters 4 and 5, the process for determining local and pore saturation in the GDL was detailed.

In Chapter 4, we visualized and quantified pore-scale liquid water accumulation in the cathode GDL of an operating PEM fuel cell, uncovering key insights into saturation behavior, including the prevalence of partially filled pores and the influence of morphology and wettability on water distribution. Using the methodology presented in Chapter 3, we imaged a custom, in-house *operando* PEM fuel cell using synchrotron X-ray CT to capture 3-D water distributions in the GDL at increasing current densities. We then isolated these distributions to investigate the way in which liquid water occupies individual pores, and how the existence of partial pores affects air transport. The key findings of this study are as follows:

1. We define and quantify *pore-scale* saturation (for the first time) in fuel cell GDLs at statistically representative scales. Partial filling of pores was observed, and pores were more saturated closer to the catalyst layer (CL)-GDL interface (43.7% saturated on

average) than at the flow field (FF)-GDL interface (27.9% saturated on average). Additionally, we found that pore saturation increased with increasing local saturation in the GDL. This trend is present at both low and high current densities and more pronounced as current density increases.

2. Higher local water saturation was observed under the land regions (86.0% of total saturation) in the GDL, where the individual pores were more saturated (19.3% under lands, 11.3% under channels). This trend appears at both low and high current densities and becomes increasingly prominent with higher current density.

3. The oftentimes default assumption of fully saturated pores in numerical models could lead to significant underestimation of GDL permeability. A GDL with partially filled pores has a 26.3% higher through-plane permeability and 50.3% higher in-plane permeability of air compared to a GDL with fully saturated pores.

The findings presented in Chapter 4 bring a new understanding to liquid water distributions in the GDL through the identification and investigation of pore-scale liquid water occupation. With these results, we can help improve the accuracy of predictions of liquid water transport by modelling techniques.

In Chapter 5, we investigated the impact of inlet gas relative humidity (RH) on local and pore saturation in the cathode GDL of an operating PEM fuel cell using operando synchrotron X-ray CT, revealing that RH significantly influences electrochemical performance, local saturation, pore-filling behavior, and water redistribution through complex interactions between capillary forces, wettability, and pathway formation. The key findings of this study are as follows:

1. At a relatively low cell temperature (60 °C), PEM fuel cell performance increases with a decrease in RH. Peak power increases by 27.4% when inlet gas RH is decreased from 100% RH to 80% RH. Maximum operating current density also increases with a decrease in RH.

2. Pore saturation tends to coincide with local saturation, where local saturation and average pore saturation both increase with RH. This affects the permeability of air through the GDL, where oxygen transport resistance increases with RH.

3. In some regions of the GDL, pore saturation decreases with an increase in relative humidity from 90% RH to 100% RH. This is attributed to the formation of new preferential liquid water pathways, which implies that water transport through the GDL is highly sensitive to local saturation conditions and capillary pressures, and that newly formed water pathways can act as drainage paths which redistribute water throughout the GDL.

The findings in Chapter 5 provide a deeper understanding of how RH influences liquid water distribution and electrochemical performance in PEM fuel cell GDLs, highlighting the critical role of pore-scale dynamics, capillary forces, and pathway formation. These insights are essential for improving numerical models and guiding the design of advanced GDL materials to optimize water management and fuel cell performance.

In conclusion, the contributions of this thesis have helped advance our understanding of the mechanisms governing liquid water transport at the pore scale in the cathode GDL of a PEM fuel cell, which is critical for optimizing water management in PEM fuel cells. By addressing these mechanisms, this work provides foundational insights that can improve the design of GDL materials and fuel cell models, enabling more efficient and reliable fuel cell operation under varying conditions.

## 6.2 Future Work

### 6.2.1 Influence of MPL on partial pore filling and drainage paths

In this study, we observed liquid water distributions in the GDL substrate material, and how partial pore filling is influenced by local saturation conditions. However, many studies have demonstrated that the addition of a microporous layer (MPL) to the GDL substrate can improve liquid water management in PEM fuel cells [97-100]. Gostick et al. used *ex-situ* measurements of water saturation and the corresponding capillary pressure at the precise moment of water breakthrough in GDL samples, both with and without an MPL [97]. They demonstrated that water breaks through the MPL at a few isolated locations at the MPL-GDL interface, and that subsequent water percolation through the GDL starts at these locations rather than the entire face of the GDL. In the measurements of GDL without an MPL, water clusters can form dead-ends in the substrate on the way to break-through at the flow channels. However, the addition of an MPL leads to far fewer dead-ends, reducing the overall liquid water saturation in the substrate.

From the conclusions of the study done in this thesis, we predict that the presence of an MPL can induce lower pore saturation in the substrate due to lower local saturations, increasing the permeability of air through the substrate and enhancing gas transport through the cathode.

Furthermore, the MPL may mitigate the need for drainage paths due to reduced local and pore saturation. Future work in this area will provide a better understanding of the role of the MPL in improved water management in GDLs and how they impact PEM fuel cell performance.

### 6.2.2 Combining measurement of internal contact angles in pores with pore saturation

In this work, we observed that higher local water saturation generally results in higher pore saturations, on average. For example, in Chapter 5, local saturation increases with RH, increasing average pore saturation. However, in some regions we observed a decrease in pore saturation with increasing RH. This effect was attributed to the formation of new, adjacent liquid water pathways that act as drainage paths for existing saturated pores. We proposed that these new pathways are formed by the following process:

1. Initial, preferential pores are saturated initially and fill to a certain threshold.
2. As the saturation in the initial pores increases with local saturation (e.g., due to increases in RH), excess water must move into neighboring pores.
3. Due to different, more favourable wettability conditions in the newly invaded pores, water begins to drain from the initially saturated pores creating a new preferential pathway.

To investigate the true nature of this phenomenon and better understand the physics which governs partial pore filling, we propose the measurement of contact angles within GDLs at different levels of local saturation.

The contact angle is the angle formed at the junction where a liquid, solid, and gas meet. It quantifies the wettability of a solid surface by a liquid and is a key parameter in understanding surface interactions. Referring to the literature presented in Chapter 2, the contact angle ($\theta$) (and thus wettability) affects capillary pressure ($P_c$) in a pore:

$$P_c = -\frac{2\gamma \cos\theta}{r} \tag{2.4}$$

where hydrophobic pores exhibit higher capillary pressure and hydrophilic pores exhibit lower capillary pressure. Thus, hydrophilic pores are more favourable to liquid water invasion. Our proposition in this study is that drainage pathways form due to lower capillary pressures induced by the changing wettability in the pores as they fill with water, since pores have been shown to exhibit mixed wettability due to heterogenous polytetrafluoroethylene (PTFE) treatments on fibres [101], [102]. Therefore, capillary pressures in the pore can change with saturation.

Lacking a reliable method for internal contact angle measurements, the fuel cell community depends on goniometer and tensiometer-based contact angle measurements corrected for the external surface morphology of the GDL (Young's contact angle), which are not accurate to actual conditions within individual pores as they assume pores to have uniform hydrophobicity. Due to the lack of direct access to the internal surfaces of the pores, measurement of the true local contact angles is challenging. AlRatrout et al. developed a computational method to calculate contact angles from segmented X-ray CT images of a porous medium filled with fluids [103]. This algorithm determines the local contact angles based on the pore space images. The contact angles reported by this method are the measured local contact angles, rather than Young's contact angles. Liu et al. applied this method to micro-X-ray CT images of water-filled commercial GDLs to calculate internal contact angles at the GDL fibre-water-air triple-phase contact point and reported the distribution of contact angles within GDLs for the first time. They used 3-D maps of the contact angles and pore sizes to simulate water transport through the pores and were able to produce results much closer to those of experimental ones compared to constant, goniometer-measured contact angles [104].

Since this work involves visualization of water in the pores with X-ray CT under varying conditions, we propose that this method for contact angle measurement be applied at different levels of GDL saturation. The result of the internal contact angle measurements can assist us in explaining the true cause of new drainage pathways for initial liquid water pathways and provide us with a deeper understanding of the mechanisms of liquid water transport in GDLs with mixed wettability.

### 6.2.3 High-speed operando tomography for liquid water pathway development

In this thesis, we studied steady-state water distributions at stabilized current densities, where initial preferential pathways have already been established. In Chapter 5, the focus of the study was directed at the differences between stable water distributions under varying RH at the same current density. While this still provides important insight into water transport mechanisms in the GDL and is useful for understanding long-term operating conditions, the study of the dynamic development of preferential liquid water pathways can provide insight into dynamic behavior, enabling the optimization of GDL design to minimize flooding, especially during start-up or fluctuating operation.

To study fast dynamics of water in the GDL, high-speed operando tomography has been employed. Recently, Dörenkamp et al. used sub-second *operando* X-ray tomographic microscopy (XTM) (high resolution X-ray CT) to study the transient development and interaction of multiple percolating water clusters in a GDL and droplet formation in the channel [105]. They demonstrated that water droplet formation and propagation is a fast process, with instabilities in droplet dynamics occurring within 3 s and channel break-through occurring in as fast as 33 s. They observed that when a droplet becomes disconnected from its feeding cluster, a sudden removal of large water volumes from the GDL to the channel can occur. This process subsequently opens intermediate pathways, enhancing reactant transport. Their work suggests that pore morphology is crucial for the stability of percolating networks within porous media. However, they did not study the effects of wettability on percolation pathways and dynamic behaviour, which also plays an important role in liquid water transport.

Knowing that droplet formation is a fast process, an area of future work that can be built from the work in this thesis is the implementation of fast operando X-ray tomography to study the initial formation of preferential pathways as well as the formation of their drainage paths. Coupling the study of dynamic and steady state liquid water transport pathways can provide a holistic understanding of water behavior in the GDL, enabling better design and management strategies for enhanced PEM fuel cell performance and longevity.

## References

[1] IEA (2024), Electricity Mid-Year Update - July 2024, IEA, Paris https://www.iea.org/reports/electricity-mid-year-update-july-2024, Licence: CC BY 4.0

[2] L. Von Bremen, “Large-Scale Variability of Weather Dependent Renewable Energy Sources,” in *Management of Weather and Climate Risk in the Energy Industry*, A. Troccoli, Ed., Dordrecht: Springer Netherlands, 2010, pp. 189–206.

[3] O. Z. Sharaf and M. F. Orhan, “An overview of fuel cell technology: Fundamentals and applications,” *Renewable and Sustainable Energy Reviews*, vol. 32, pp. 810–853, 2014, doi: https://doi.org/10.1016/j.rser.2014.01.012.

[4] Natural Resources Canada (2023) Energy efficiency for transportation and alternative fuels.

[5] D. A. Cullen *et al.*, “New roads and challenges for fuel cells in heavy-duty transportation,” *Nat Energy*, vol. 6, no. 5, pp. 462–474, 2021, doi: 10.1038/s41560-021-00775-z.

[6] N. Sazali, W. Norharyati, A. S. Jamaludin, and M. Razali, “New Perspectives on Fuel Cell Technology: A Brief Review,” *Membranes (Basel)*, vol. 10, p. 99, May 2020, doi: 10.3390/membranes10050099.

[7] Q. Tang, B. Li, D. Yang, P. Ming, C. Zhang, and Y. Wang, “Review of hydrogen crossover through the polymer electrolyte membrane,” *Int J Hydrogen Energy*, vol. 46, no. 42, pp. 22040–22061, 2021, doi: https://doi.org/10.1016/j.ijhydene.2021.04.050.

[8] Y. Tang, A. Kusoglu, A. M. Karlsson, M. H. Santare, S. Cleghorn, and W. B. Johnson, “Mechanical properties of a reinforced composite polymer electrolyte membrane and its

simulated performance in PEM fuel cells," *J Power Sources*, vol. 175, no. 2, pp. 817–825, 2008, doi: https://doi.org/10.1016/j.jpowsour.2007.09.093.

[9] S. Ahmad, T. Nawaz, A. Ali, M. F. Orhan, A. Samreen, and A. M. Kannan, "An overview of proton exchange membranes for fuel cells: Materials and manufacturing," *Int J Hydrogen Energy*, vol. 47, no. 44, pp. 19086–19131, 2022, doi: https://doi.org/10.1016/j.ijhydene.2022.04.099.

[10] P. Schneider *et al.*, "Impact of Platinum Loading and Layer Thickness on Cathode Catalyst Degradation in PEM Fuel Cells," *J Electrochem Soc*, vol. 170, no. 2, p. 024506, 2023, doi: 10.1149/1945-7111/acb8df.

[11] S. Park, J.-W. Lee, and B. N. Popov, "A review of gas diffusion layer in PEM fuel cells: Materials and designs," *Int J Hydrogen Energy*, vol. 37, no. 7, pp. 5850–5865, 2012, doi: https://doi.org/10.1016/j.ijhydene.2011.12.148.

[12] K. Jiao and X. Li, "Water transport in polymer electrolyte membrane fuel cells," *Prog Energy Combust Sci*, vol. 37, no. 3, pp. 221–291, 2011, doi: https://doi.org/10.1016/j.pecs.2010.06.002.

[13] A. H. Kakaee, G. R. Molaeimanesh, and M. H. Elyasi Garmaroudi, "Impact of PTFE distribution across the GDL on the water droplet removal from a PEM fuel cell electrode containing binder," *Int J Hydrogen Energy*, vol. 43, no. 32, pp. 15481–15491, 2018, doi: https://doi.org/10.1016/j.ijhydene.2018.06.111.

[14] R. W. I. I. I. Atkinson, Y. Garsany, B. D. Gould, K. E. Swider-Lyons, and I. V Zenyuk, "The Role of Compressive Stress on Gas Diffusion Media Morphology and Fuel Cell

Performance," *ACS Appl Energy Mater*, vol. 1, no. 1, pp. 191–201, Jan. 2018, doi: 10.1021/acsaem.7b00077.

[15] A. Bazylak, J. Heinrich, N. Djilali, and D. Sinton, "Liquid water transport between graphite paper and a solid surface," *J Power Sources*, vol. 185, no. 2, pp. 1147–1153, 2008, doi: https://doi.org/10.1016/j.jpowsour.2008.07.031.

[16] S. Litster, D. Sinton, and N. Djilali, "Ex situ visualization of liquid water transport in PEM fuel cell gas diffusion layers," *J Power Sources*, vol. 154, no. 1, pp. 95–105, 2006, doi: https://doi.org/10.1016/j.jpowsour.2005.03.199.

[17] S. Y. Jung and M. Mortazavi, "Transient characteristics of in-plane water transport in gas diffusion layers of PEM fuel cells," *Int J Hydrogen Energy*, vol. 51, pp. 1584–1593, 2024, doi: https://doi.org/10.1016/j.ijhydene.2023.10.055.

[18] J. H. Nam and M. Kaviany, "Effective diffusivity and water-saturation distribution in single- and two-layer PEMFC diffusion medium," *Int J Heat Mass Transf*, vol. 46, no. 24, pp. 4595–4611, 2003, doi: https://doi.org/10.1016/S0017-9310(03)00305-3.

[19] U. Pasaogullari and C. Y. Wang, "Liquid Water Transport in Gas Diffusion Layer of Polymer Electrolyte Fuel Cells," *J Electrochem Soc*, vol. 151, no. 3, p. A399, 2004, doi: 10.1149/1.1646148.

[20] A. Bazylak, D. Sinton, Z.-S. Liu, and N. Djilali, "Effect of compression on liquid water transport and microstructure of PEMFC gas diffusion layers," *J Power Sources*, vol. 163, no. 2, pp. 784–792, 2007, doi: https://doi.org/10.1016/j.jpowsour.2006.09.045.

[21] M. Li, S. Foroughi, J. Zhao, B. Bijeljic, and M. J. Blunt, “Image-based pore-scale modelling of the effect of wettability on breakthrough capillary pressure in gas diffusion layers,” *J Power Sources*, vol. 584, p. 233539, 2023, doi: https://doi.org/10.1016/j.jpowsour.2023.233539.

[22] F. Jinuntuya, M. Whiteley, R. Chen, and A. Fly, “The effects of gas diffusion layers structure on water transportation using X-ray computed tomography based Lattice Boltzmann method,” *J Power Sources*, vol. 378, pp. 53–65, 2018, doi: https://doi.org/10.1016/j.jpowsour.2017.12.016.

[23] A. Z. Weber and J. Newman, “Coupled Thermal and Water Management in Polymer Electrolyte Fuel Cells,” *J Electrochem Soc*, vol. 153, no. 12, p. A2205, 2006, doi: 10.1149/1.2352039.

[24] N. Djilali and D. Lu, “Influence of heat transfer on gas and water transport in fuel cells,” *International Journal of Thermal Sciences*, vol. 41, no. 1, pp. 29–40, 2002, doi: https://doi.org/10.1016/S1290-0729(01)01301-1.

[25] A. M. F. R. Pinto, V. B. Oliveira, and D. S. Falcão, “4 - Experimental methods of characterization,” in *Direct Alcohol Fuel Cells for Portable Applications*, A. M. F. R. Pinto, V. B. Oliveira, and D. S. Falcão, Eds., Academic Press, 2018, pp. 113–155. doi: https://doi.org/10.1016/B978-0-12-811849-8.00004-8.

[26] M. M. Mench, *Fuel cell engines*. John Wiley & Sons, 2008.

[27] O. S. Burheim, H. Su, S. Pasupathi, J. G. Pharoah, and B. G. Pollet, “Thermal conductivity and temperature profiles of the micro porous layers used for the polymer electrolyte

membrane fuel cell," *Int J Hydrogen Energy*, vol. 38, no. 20, pp. 8437–8447, 2013, doi: https://doi.org/10.1016/j.ijhydene.2013.04.140.

[28] A. Thomas, G. Maranzana, S. Didierjean, J. Dillet, and O. Lottin, "Thermal and water transfer in PEMFCs: Investigating the role of the microporous layer," *Int J Hydrogen Energy*, vol. 39, no. 6, pp. 2649–2658, 2014, doi: https://doi.org/10.1016/j.ijhydene.2013.11.105.

[29] N. Zamel, J. Becker, and A. Wiegmann, "Estimating the thermal conductivity and diffusion coefficient of the microporous layer of polymer electrolyte membrane fuel cells," *J Power Sources*, vol. 207, pp. 70–80, 2012, doi: https://doi.org/10.1016/j.jpowsour.2012.02.003.

[30] U. Pasaogullari and C.-Y. Wang, "Two-phase transport and the role of micro-porous layer in polymer electrolyte fuel cells," *Electrochim Acta*, vol. 49, no. 25, pp. 4359–4369, 2004, doi: https://doi.org/10.1016/j.electacta.2004.04.027.

[31] A. Kato *et al.*, "Operando X-ray radiography of liquid water distribution in 100 mm polymer electrolyte fuel cell channels," *Electrochem commun*, vol. 165, p. 107772, 2024, doi: https://doi.org/10.1016/j.elecom.2024.107772.

[32] J. Lee, J. Hinebaugh, and A. Bazylak, "Synchrotron X-ray radiographic investigations of liquid water transport behavior in a PEMFC with MPL-coated GDLs," *J Power Sources*, vol. 227, pp. 123–130, 2013, doi: https://doi.org/10.1016/j.jpowsour.2012.11.006.

[33] H. Liu *et al.*, "Microporous Layer Degradation in Polymer Electrolyte Membrane Fuel Cells," *J Electrochem Soc*, vol. 165, no. 6, p. F3271, 2018, doi: 10.1149/2.0291806jes.

[34] R. Banerjee *et al.*, “Transient Liquid Water Distributions in Polymer Electrolyte Membrane Fuel Cell Gas Diffusion Layers Observed through In-Operando Synchrotron X-ray Radiography,” *J Electrochem Soc*, vol. 164, no. 2, p. F154, 2017, doi: 10.1149/2.0991702jes.

[35] J. Hinebaugh, J. Lee, and A. Bazylak, “Visualizing Liquid Water Evolution in a PEM Fuel Cell Using Synchrotron X-ray Radiography,” *J Electrochem Soc*, vol. 159, no. 12, p. F826, 2012, doi: 10.1149/2.054212jes.

[36] P. Antonacci, S. Chevalier, J. Lee, R. Yip, N. Ge, and A. Bazylak, “Feasibility of combining electrochemical impedance spectroscopy and synchrotron X-ray radiography for determining the influence of liquid water on polymer electrolyte membrane fuel cell performance,” *Int J Hydrogen Energy*, vol. 40, no. 46, pp. 16494–16502, 2015, doi: https://doi.org/10.1016/j.ijhydene.2015.10.008.

[37] A. Pfrang, D. Veyret, F. Sieker, and G. Tsotridis, “X-ray computed tomography of gas diffusion layers of PEM fuel cells: Calculation of thermal conductivity,” *Int J Hydrogen Energy*, vol. 35, no. 8, pp. 3751–3757, 2010, doi: https://doi.org/10.1016/j.ijhydene.2010.01.085.

[38] H. Ostadi, P. Rama, Y. Liu, R. Chen, X. X. Zhang, and K. Jiang, “Influence of threshold variation on determining the properties of a polymer electrolyte fuel cell gas diffusion layer in X-ray nano-tomography,” *Chem Eng Sci*, vol. 65, no. 6, pp. 2213–2217, 2010, doi: https://doi.org/10.1016/j.ces.2009.12.019.

[39] A. Pfrang, D. Veyret, G. J. M. Janssen, and G. Tsotridis, “Imaging of membrane electrode assemblies of proton exchange membrane fuel cells by X-ray computed tomography,” *J*

*Power Sources*, vol. 196, no. 12, pp. 5272–5276, 2011, doi: https://doi.org/10.1016/j.jpowsour.2010.09.020.

[40] A. Pfrang, S. Didas, and G. Tsotridis, "X-ray computed tomography of gas diffusion layers of PEM fuel cells: Segmentation of the microporous layer," *J Power Sources*, vol. 235, pp. 81–86, 2013, doi: https://doi.org/10.1016/j.jpowsour.2013.01.179.

[41] Ph. Krüger *et al.*, "Synchrotron X-ray tomography for investigations of water distribution in polymer electrolyte membrane fuel cells," *J Power Sources*, vol. 196, no. 12, pp. 5250–5255, 2011, doi: https://doi.org/10.1016/j.jpowsour.2010.09.042.

[42] J. Eller, J. Roth, F. Marone, M. Stampanoni, and F. N. Büchi, "Operando Properties of Gas Diffusion Layers: Saturation and Liquid Permeability," *J Electrochem Soc*, vol. 164, no. 2, p. F115, 2017, doi: 10.1149/2.0881702jes.

[43] T. and S. Dörenkamp Mayank and Marone Federica and Buchi Felix N. and Schmidt Thomas J. and Eller Jens, "Investigation of Dynamic Water Cluster and Droplet Interactions in Polymer Electrolyte Fuel Cells using Operando X-ray Tomographic Microscopy," *J Electrochem Soc*, 2024, [Online]. Available: http://iopscience.iop.org/article/10.1149/1945-7111/ad749f

[44] J. T. Gostick, "Versatile and efficient pore network extraction method using marker-based watershed segmentation," *Phys Rev E*, vol. 96, no. 2, p. 23307, Aug. 2017, doi: 10.1103/PhysRevE.96.023307.

[45] B. Gackiewicz, K. Lamorski, C. Sławiński, S.-Y. Hsu, and L.-C. Chang, "An intercomparison of the pore network to the Navier–Stokes modeling approach applied for

saturated conductivity estimation from X-ray CT images," *Sci Rep*, vol. 11, no. 1, p. 5859, 2021, doi: 10.1038/s41598-021-85325-z.

[46] T. G. Tranter, J. T. Gostick, A. D. Burns, and W. F. Gale, "Pore Network Modeling of Compressed Fuel Cell Components with OpenPNM," *Fuel Cells*, vol. 16, no. 4, pp. 504–515, Aug. 2016, doi: https://doi.org/10.1002/fuce.201500168.

[47] M. Shahraeeni, "Study of fluid flow in the porous media of gas diffusion layers in proton exchange membrane fuel cells," 2013. [Online]. Available: https://open.library.ubc.ca/collections/24/items/1.0073812

[48] M. Shahraeeni and M. Hoorfar, "Experimental and numerical comparison of water transport in untreated and treated diffusion layers of proton exchange membrane (PEM) fuel cells," *J Power Sources*, vol. 238, pp. 29–47, 2013, doi: https://doi.org/10.1016/j.jpowsour.2013.03.023.

[49] M. Shahraeeni and M. Hoorfar, "Pore-network modeling of liquid water flow in gas diffusion layers of proton exchange membrane fuel cells," *Int J Hydrogen Energy*, vol. 39, no. 20, pp. 10697–10709, 2014, doi: https://doi.org/10.1016/j.ijhydene.2014.05.017.

[50] M. Aghighi and J. Gostick, "Pore network modeling of phase change in PEM fuel cell fibrous cathode," *J Appl Electrochem*, vol. 47, no. 12, pp. 1323–1338, 2017, doi: 10.1007/s10800-017-1126-6.

[51] H. Nakajima, S. Iwasaki, and T. Kitahara, "Pore network modeling of a microporous layer for polymer electrolyte fuel cells under wet conditions," *J Power Sources*, vol. 560, p. 232677, 2023, doi: https://doi.org/10.1016/j.jpowsour.2023.232677.

[52] T. W. Wysokinski, D. Chapman, G. Adams, M. Renier, P. Suortti, and W. Thomlinson, "Beamlines of the biomedical imaging and therapy facility at the Canadian light source—Part 1," *Nucl Instrum Methods Phys Res A*, vol. 582, no. 1, pp. 73–76, 2007, doi: https://doi.org/10.1016/j.nima.2007.08.087.

[53] J. Sim, M. Kang, K. Min, E. Lee, and J.-Y. Jyoung, "Effects of carbon corrosion on proton exchange membrane fuel cell performance using two durability evaluation methods," *Renew Energy*, vol. 190, pp. 959–970, 2022, doi: https://doi.org/10.1016/j.renene.2022.04.015.

[54] J. Zhao, Z. Tu, and S. H. Chan, "Carbon corrosion mechanism and mitigation strategies in a proton exchange membrane fuel cell (PEMFC): A review," *J Power Sources*, vol. 488, p. 229434, 2021, doi: https://doi.org/10.1016/j.jpowsour.2020.229434.

[55] Y. Qin, Q. Du, Y. Yin, K. Jiao, and X. Li, "Numerical investigation of water dynamics in a novel proton exchange membrane fuel cell flow channel," *J Power Sources*, vol. 222, pp. 150–160, 2013, doi: https://doi.org/10.1016/j.jpowsour.2012.07.084.

[56] K. Jiao, J. Park, and X. Li, "Experimental investigations on liquid water removal from the gas diffusion layer by reactant flow in a PEM fuel cell," *Appl Energy*, vol. 87, no. 9, pp. 2770–2777, 2010, doi: https://doi.org/10.1016/j.apenergy.2009.04.041.

[57] P. Shrestha, C. H. Lee, K. F. Fahy, M. Balakrishnan, N. Ge, and A. Bazylak, "Formation of Liquid Water Pathways in PEM Fuel Cells: A 3-D Pore-Scale Perspective," *J Electrochem Soc*, vol. 167, no. 5, p. 054516, 2020, doi: 10.1149/1945-7111/ab7a0b.

[58] T. J. Mason, J. Millichamp, T. P. Neville, A. El-kharouf, B. G. Pollet, and D. J. L. Brett, "Effect of clamping pressure on ohmic resistance and compression of gas diffusion layers

for polymer electrolyte fuel cells," *J Power Sources*, vol. 219, pp. 52–59, 2012, doi: https://doi.org/10.1016/j.jpowsour.2012.07.021.

[59] T. J. Mason, J. Millichamp, P. R. Shearing, and D. J. L. Brett, "A study of the effect of compression on the performance of polymer electrolyte fuel cells using electrochemical impedance spectroscopy and dimensional change analysis," *Int J Hydrogen Energy*, vol. 38, no. 18, pp. 7414–7422, 2013, doi: https://doi.org/10.1016/j.ijhydene.2013.04.021.

[60] S. G. Kandlikar, Z. Lu, T. Y. Lin, D. Cooke, and M. Daino, "Uneven gas diffusion layer intrusion in gas channel arrays of proton exchange membrane fuel cell and its effects on flow distribution," *J Power Sources*, vol. 194, no. 1, pp. 328–337, 2009, doi: https://doi.org/10.1016/j.jpowsour.2009.05.019.

[61] T. Faragó *et al.*, " Tofu: a fast, versatile and user-friendly image processing toolkit for computed tomography," *J Synchrotron Radiat*, vol. 29, no. 3, pp. 916–927, May 2022, doi: 10.1107/S160057752200282X.

[62] D. Paganin, S. C. Mayo, T. E. Gureyev, P. R. Miller, and S. W. Wilkins, "Simultaneous phase and amplitude extraction from a single defocused image of a homogeneous object," *J Microsc*, vol. 206, no. 1, pp. 33–40, Apr. 2002, doi: https://doi.org/10.1046/j.1365-2818.2002.01010.x.

[63] B. Nett, "Filtered BackProjection (FBP) Illustrated Guide for Radiologic Technologists." Accessed: Dec. 18, 2024. [Online]. Available: https://howradiologyworks.com/filtered-backprojection-fbp-illustrated-guide-for-radiologic-technologists/

[64] C. A. Schneider, W. S. Rasband, and K. W. Eliceiri, "NIH Image to ImageJ: 25 years of image analysis," *Nat Methods*, vol. 9, no. 7, pp. 671–675, 2012, doi: 10.1038/nmeth.2089.

[65] I. V Zenyuk, D. Y. Parkinson, L. G. Connolly, and A. Z. Weber, “Gas-diffusion-layer structural properties under compression via X-ray tomography,” *J Power Sources*, vol. 328, pp. 364–376, 2016, doi: https://doi.org/10.1016/j.jpowsour.2016.08.020.

[66] Dragonfly 2022.2 [Computer software]. Comet Technologies Canada Inc., Montreal, Canada; software available at https://www.theobjects.com/dragonfly.

[67] NumFOCUS, “DemonsRegistration1.” simpleitk.readthedocs.io. https://simpleitk.readthedocs.io/en/master/link_DemonsRegistration1_docs.html (accessed Jun. 17, 2024)

[68] T. Y. Goh, S. N. Basah, H. Yazid, M. J. Aziz Safar, and F. S. Ahmad Saad, “Performance analysis of image thresholding: Otsu technique,” *Measurement*, vol. 114, pp. 298–307, 2018, doi: https://doi.org/10.1016/j.measurement.2017.09.052.

[69] C. Sha, J. Hou, and H. Cui, “A robust 2D Otsu’s thresholding method in image segmentation,” *J Vis Commun Image Represent*, vol. 41, pp. 339–351, 2016, doi: https://doi.org/10.1016/j.jvcir.2016.10.013.

[70] X. Xu, S. Xu, L. Jin, and E. Song, “Characteristic analysis of Otsu threshold and its applications,” *Pattern Recognit Lett*, vol. 32, no. 7, pp. 956–961, 2011, doi: https://doi.org/10.1016/j.patrec.2011.01.021.

[71] Z. Hou, Q. Hu, and W. L. Nowinski, “On minimum variance thresholding,” *Pattern Recognit Lett*, vol. 27, no. 14, pp. 1732–1743, 2006, doi: https://doi.org/10.1016/j.patrec.2006.04.012.

[72] M. Sezgin and B. Sankur, "Survey over image thresholding techniques and quantitative performance evaluation," *J Electron Imaging*, vol. 13, no. 1, pp. 146–165, Jan. 2004, doi: 10.1117/1.1631315.

[73] N. Otsu, "A Threshold Selection Method from Gray-Level Histograms," *IEEE Trans Syst Man Cybern*, vol. 9, no. 1, pp. 62–66, 1979, doi: 10.1109/TSMC.1979.4310076.

[74] G. Athanasaki, A. Jayakumar, and A. M. Kannan, "Gas diffusion layers for PEM fuel cells: Materials, properties and manufacturing – A review," *Int J Hydrogen Energy*, vol. 48, no. 6, pp. 2294–2313, 2023, doi: https://doi.org/10.1016/j.ijhydene.2022.10.058.

[75] F. Cai, S. Cai, and Z. Tu, "Proton exchange membrane fuel cell (PEMFC) operation in high current density (HCD): Problem, progress and perspective," *Energy Convers Manag*, vol. 307, p. 118348, 2024, doi: https://doi.org/10.1016/j.enconman.2024.118348.

[76] R. Guan, P. Shrestha, J. K. Lee, and A. Bazylak, "Determining local transport properties of gas diffusion layer land-channel regions via pore network modelling," *J Power Sources*, vol. 562, p. 232770, 2023, doi: https://doi.org/10.1016/j.jpowsour.2023.232770.

[77] P. Shrestha, C. H. Lee, K. F. Fahy, M. Balakrishnan, N. Ge, and A. Bazylak, "Formation of Liquid Water Pathways in PEM Fuel Cells: A 3-D Pore-Scale Perspective," *J Electrochem Soc*, vol. 167, no. 5, p. 054516, 2020, doi: 10.1149/1945-7111/ab7a0b.

[78] F. Wiesner *et al.*, "Unveiling the Role of PTFE Surface Coverage on Controlling Gas Diffusion Layer Water Content," *ACS Appl Mater Interfaces*, vol. 16, no. 27, pp. 34947–34961, Jul. 2024, doi: 10.1021/acsami.4c04641.

[79] J. Gostick *et al.*, “OpenPNM: A Pore Network Modeling Package,” *Comput Sci Eng*, vol. 18, no. 4, pp. 60–74, 2016, doi: 10.1109/MCSE.2016.49.

[80] J. Zhang *et al.*, “PEM fuel cell relative humidity (RH) and its effect on performance at high temperatures,” *Electrochim Acta*, vol. 53, no. 16, pp. 5315–5321, 2008, doi: https://doi.org/10.1016/j.electacta.2008.02.074.

[81] P. Deevanhxay, T. Sasabe, S. Tsushima, and S. Hirai, “Investigation of water accumulation and discharge behaviors with variation of current density in PEMFC by high-resolution soft X-ray radiography,” *Int J Hydrogen Energy*, vol. 36, no. 17, pp. 10901–10907, 2011, doi: https://doi.org/10.1016/j.ijhydene.2011.05.160.

[82] J. Eller, J. Roth, F. Marone, M. Stampanoni, A. Wokaun, and F. N. Büchi, “Implications of polymer electrolyte fuel cell exposure to synchrotron radiation on gas diffusion layer water distribution,” *J Power Sources*, vol. 245, pp. 796–800, 2014, doi: https://doi.org/10.1016/j.jpowsour.2013.07.025.

[83] T. Reshetenko and A. Kulikovsky, “A quasi three–dimensional model for PEM fuel cell impedance: The effect of local oxygen depletion under the flow field rib,” *Mater Res Express*, vol. 10, no. 11, p. 115504, 2023, doi: 10.1088/2053-1591/ad09a6.

[84] P. Rama *et al.*, “A Numerical Study of Structural Change and Anisotropic Permeability in Compressed Carbon Cloth Polymer Electrolyte Fuel Cell Gas Diffusion Layers,” *Fuel Cells*, vol. 11, no. 2, pp. 274–285, Apr. 2011, doi: https://doi.org/10.1002/fuce.201000037.

[85] R. W. I. I. I. Atkinson, Y. Garsany, B. D. Gould, K. E. Swider-Lyons, and I. V Zenyuk, “The Role of Compressive Stress on Gas Diffusion Media Morphology and Fuel Cell

Performance," *ACS Appl Energy Mater*, vol. 1, no. 1, pp. 191–201, Jan. 2018, doi: 10.1021/acsaem.7b00077.

[86] M. Li, S. Foroughi, J. Zhao, B. Bijeljic, and M. J. Blunt, "Image-based pore-scale modelling of the effect of wettability on breakthrough capillary pressure in gas diffusion layers," *J Power Sources*, vol. 584, p. 233539, 2023, doi: https://doi.org/10.1016/j.jpowsour.2023.233539.

[87] F. Jinuntuya, M. Whiteley, R. Chen, and A. Fly, "The effects of gas diffusion layers structure on water transportation using X-ray computed tomography based Lattice Boltzmann method," *J Power Sources*, vol. 378, pp. 53–65, 2018, doi: https://doi.org/10.1016/j.jpowsour.2017.12.016.

[88] J. Zhang *et al.*, "PEM fuel cell relative humidity (RH) and its effect on performance at high temperatures," *Electrochim Acta*, vol. 53, no. 16, pp. 5315–5321, 2008, doi: https://doi.org/10.1016/j.electacta.2008.02.074.

[89] J.-H. Jang, W.-M. Yan, H.-Y. Li, and Y.-C. Chou, "Humidity of reactant fuel on the cell performance of PEM fuel cell with baffle-blocked flow field designs," *J Power Sources*, vol. 159, no. 1, pp. 468–477, 2006, doi: https://doi.org/10.1016/j.jpowsour.2005.07.096.

[90] L. Wang, A. Husar, T. Zhou, and H. Liu, "A parametric study of PEM fuel cell performances," *Int J Hydrogen Energy*, vol. 28, no. 11, pp. 1263–1272, 2003, doi: https://doi.org/10.1016/S0360-3199(02)00284-7.

[91] R. Jiang, H. R. Kunz, and J. M. Fenton, "Investigation of membrane property and fuel cell behavior with sulfonated poly(ether ether ketone) electrolyte: Temperature and relative

humidity effects," *J Power Sources*, vol. 150, pp. 120–128, 2005, doi: https://doi.org/10.1016/j.jpowsour.2005.03.180.

[92] M. M. Saleh, T. Okajima, M. Hayase, F. Kitamura, and T. Ohsaka, "Exploring the effects of symmetrical and asymmetrical relative humidity on the performance of H2/air PEM fuel cell at different temperatures," *J Power Sources*, vol. 164, no. 2, pp. 503–509, 2007, doi: https://doi.org/10.1016/j.jpowsour.2006.11.065.

[93] A. V Anantaraman and C. L. Gardner, "Studies on ion-exchange membranes. Part 1. Effect of humidity on the conductivity of Nafion®," *Journal of Electroanalytical Chemistry*, vol. 414, no. 2, pp. 115–120, 1996, doi: https://doi.org/10.1016/0022-0728(96)04690-6.

[94] Y.-C. Chen *et al.*, "On the water transport mechanism through the microporous layers of operando polymer electrolyte fuel cells probed directly by X-ray tomographic microscopy," *Energy Advances*, vol. 2, no. 9, pp. 1447–1463, 2023, doi: 10.1039/D3YA00189J.

[95] J. Gostick *et al.*, "OpenPNM: A Pore Network Modeling Package," *Comput Sci Eng*, vol. 18, no. 4, pp. 60–74, 2016, doi: 10.1109/MCSE.2016.49.

[96] T. Y. Goh, S. N. Basah, H. Yazid, M. J. Aziz Safar, and F. S. Ahmad Saad, "Performance analysis of image thresholding: Otsu technique," *Measurement*, vol. 114, pp. 298–307, 2018, doi: https://doi.org/10.1016/j.measurement.2017.09.052.

[97] J. T. Gostick, M. A. Ioannidis, M. W. Fowler, and M. D. Pritzker, "On the role of the microporous layer in PEMFC operation," *Electrochem commun*, vol. 11, no. 3, pp. 576–579, 2009, doi: https://doi.org/10.1016/j.elecom.2008.12.053.

[98] A. Mohseninia *et al.*, “Enhanced Water Management in PEMFCs: Perforated Catalyst Layer and Microporous Layers,” *ChemSusChem*, vol. 13, no. 11, pp. 2931–2934, Jun. 2020, doi: https://doi.org/10.1002/cssc.202000542.

[99] Y.-C. Chen *et al.*, “On the water transport mechanism through the microporous layers of operando polymer electrolyte fuel cells probed directly by X-ray tomographic microscopy,” *Energy Advances*, vol. 2, no. 9, pp. 1447–1463, 2023, doi: 10.1039/D3YA00189J.

[100] Q. Yin *et al.*, “The buffer microporous layer improved water management for proton exchange membrane fuel cell at varying humidification,” *Journal of Electroanalytical Chemistry*, vol. 928, p. 117072, 2023, doi: https://doi.org/10.1016/j.jelechem.2022.117072.

[101] Z. Fishman and A. Bazylak, “Heterogeneous Through-Plane Porosity Distributions for Treated PEMFC GDLs I. PTFE Effect,” *J Electrochem Soc*, vol. 158, no. 8, p. B841, 2011, doi: 10.1149/1.3594578.

[102] Z. Fishman and A. Bazylak, “Heterogeneous Through-Plane Porosity Distributions for Treated PEMFC GDLs. II. Effect of MPL Cracks,” *J Electrochem Soc*, vol. 158, no. 8, p. B846, 2011, doi: 10.1149/1.3594636.

[103] A. AlRatrout, A. Q. Raeini, B. Bijeljic, and M. J. Blunt, “Automatic measurement of contact angle in pore-space images,” *Adv Water Resour*, vol. 109, pp. 158–169, 2017, doi: https://doi.org/10.1016/j.advwatres.2017.07.018.

[104] C. P. Liu, P. Saha, Y. Huang, S. Shimpalee, P. Satjaritanun, and I. V Zenyuk, “Measurement of Contact Angles at Carbon Fiber–Water–Air Triple-Phase Boundaries Inside Gas Diffusion Layers Using X-ray Computed Tomography,” *ACS Appl Mater Interfaces*, vol. 13, no. 17, pp. 20002–20013, May 2021, doi: 10.1021/acsami.1c00849.

[105] T. Dörenkamp, M. Sabharwal, F. Marone, F. N. Büchi, T. J. Schmidt, and J. Eller, "Investigation of Dynamic Water Cluster and Droplet Interactions in Polymer Electrolyte Fuel Cells using Operando X-ray Tomographic Microscopy," *J Electrochem Soc*, vol. 171, no. 9, p. 094505, 2024, doi: 10.1149/1945-7111/ad749f.